universität wien

MASTERARBEIT / MASTER'S THESIS

Titel der Masterarbeit / Title of the Master's Thesis

Nonlinear Optics with Graphene

verfasst von / submitted by

Hlib Bieliaiev, BSc

angestrebter akademischer Grad / in partial fulfilment of the requirements for the degree of

Master of Science (MSc)

Wien, 2021 / Vienna, 2021

Studienkennzahl lt. Studienblatt / degree programme code as it appears on the student record sheet:	A 066 876
Studienrichtung lt. Studienblatt / degree programme as it appears on the student record sheet:	Masterstudium Physik
Betreut von / Supervisor:	Univ.-Prof. Dipl.-Ing. Dr. Philip Walther

Abstract

One of the most well-known 2D-materials is graphene. Its band structure is unique even among its own group. Several remarkable properties originate from its band structure: linear energy dispersion, universal linear conductivity and frequency-independent optical absorption for example. Also, its electrons have constant speed that only depends on the direction of the k-vector. This last property makes graphene particularly attractive for nonlinear optics.

Photons don't interact under normal conditions, but they may interact if one confines them to a volume small enough in a nonlinear medium for a sufficiently long time (1). Having photons interact in a nonlinear medium with sufficient probability could lead to the creation of graphene-based quantum logic gates for a quantum computer (2).

Applying electrostatic gating one can continuously tune electronic and thus optical properties of graphene. This allows us to control the optical resonance of material, increasing its optical response, thus empowering the interaction. Using the capacitor model from high-school physics we can describe and visualize the effects of this technique. A major result of this thesis is the development of a protocol to realize this technique experimentally, allowing our group to now to create and characterize graphene-based electro-optic devices for use in our nonlinear optical experiments.

So far the third-order nonlinearity has been primarily studied in graphene, which has started to lead to the investigation of other nonlinearities. So far, there have been just a few reports of higher-order effects, mostly in few-layer graphene. Also, these experiments are typically carried out in the THz spectral region or mid-infrared and rely on pump light of ultra-high fluence, which is a regime our lab cannot currently reach. Our initial goal was to study higher-order effects experimentally in near-infrared wavelengths, but due to experimental challenges, we decided to first focus on the theory. This thesis will also present the results of three simulations that I developed towards this goal.

Our overall research goals focus on nonlinear signal generation in near-infrared to telecom wavelengths in monolayer graphene at low optical power. To get there, we also study the effects of metal nanostructures on electrostatically doped graphene devices to enhance the nonlinear response. This thesis will also present my contributions in this experiment.

Over the last three years, I participated in various research projects and made diverse contributions, including simulations, nonlinear optical measurements, spectroscopy, and sample preparation.

The theoretical models, that I implemented and made interactive with the help of computer simulations, have now become the basis of our research, since every new project and every new optical setup now begins with predicting, finding, and measuring the third-harmonic signal. With my simulations of fifth-order nonlinear current, we can now model the nonlinear response of undoped samples to incident pump light. The electron temperature, which plays a key role when measuring sharp transition resonances, has become more approachable with available simulations.

The procedure I developed to prepare devices for graphene gating will allow us to investigate graphene nonlinearities far beyond the near-infrared spectral region due to their extreme tunability. Now the samples can be prepared and fully characterized within just two working days inside our optical lab.

Zusammenfassung

Eines der bekanntesten 2D-Materialien ist Graphen. Die Bandstruktur ist selbst in der eigenen Gruppe einzigartig. Einige bemerkenswerte Eigenschaften ergeben sich aus seiner Bandstruktur: lineare Energiedispersion, universelle lineare Leitfähigkeit und frequenzunabhängige optische Absorption zum Beispiel. Außerdem haben seine Elektronen eine konstante Geschwindigkeit, die nur von der Richtung des k-Vektors abhängt. Diese letzte Eigenschaft macht Graphen besonders attraktiv für die nichtlineare Optik.

Photonen wechselwirken unter normalen Bedingungen nicht, aber sie können wechselwirken, wenn man sie für eine ausreichend lange Zeit in einem nichtlinearen Medium auf ein Volumen beschränkt, das klein genug ist (1). Wenn Photonen mit ausreichender Wahrscheinlichkeit in einem nichtlinearen Medium wechselwirken, können graphenbasierte Quantenlogikgatter für einen Quantencomputer (2) erstellt werden.

Durch elektrostatisches Gating können die elektronischen und damit optischen Eigenschaften von Graphen kontinuierlich eingestellt werden. Dies ermöglicht uns, die optische Resonanz des Materials zu steuern, seine optische Empfindlichkeit zu erhöhen und so die Wechselwirkung zu stärken. Mit dem Kondensatormodell aus der Hochschulphysik können wir die Auswirkungen dieser Technik beschreiben und visualisieren. Das Hauptergebnis dieser Arbeit ist die Entwicklung eines Protokolls zur experimentellen Realisierung dieser Technik, mit dem unsere Gruppe nun elektrooptische Geräte auf Graphenbasis für die Verwendung in unseren nichtlinearen optischen Experimenten erstellen und charakterisieren kann.

Bisher wurde die Nichtlinearität dritter Ordnung hauptsächlich in Graphen untersucht, was zur Untersuchung anderer Nichtlinearitäten führte. Bisher gab es nur wenige Berichte über Effekte höherer Ordnung, hauptsächlich in Graphen mit wenigen Schichten. Diese Experimente werden typischerweise im THz-Spektralbereich oder im mittleren Infrarot durchgeführt und basieren auf Pumplicht mit ultrahoher Strahlungsdichte, ein Regime, das unser Labor derzeit nicht erreichen kann. Unser ursprüngliches Ziel war es, Effekte höherer Ordnung experimentell in Wellenlängen im nahen Infrarot zu untersuchen. Aufgrund experimenteller Herausforderungen beschlossen wir jedoch, uns zunächst auf die Theorie zu konzentrieren. Diese Arbeit wird auch die Ergebnisse von drei Simulationen präsentieren, die ich in Richtung auf dieses Ziel entwickelt habe.

Unsere allgemeinen Forschungsziele konzentrieren sich auf die nichtlineare Signalerzeugung im nahen Infrarot bis zur Telekommunikationswellenlänge in Monoschichtgraphen bei geringer optischer Leistung. Um dorthin zu gelangen, untersuchen wir auch die Auswirkungen von Metallnanostrukturen auf elektrostatisch dotierte Graphenvorrichtungen, um die nichtlineare Reaktion zu verbessern. Diese Arbeit wird auch meine Beiträge in diesem Experiment präsentieren.

In den letzten drei Jahren habe ich an verschiedenen Forschungsprojekten teilgenommen und verschiedene Beiträge geleistet, darunter Simulationen, nichtlineare optische Messungen, Spektroskopie und Probenvorbereitung.

Die theoretischen Modelle, die ich mithilfe von Computersimulationen implementiert und interaktiv gemacht habe, sind nun die Grundlage unserer Forschung geworden, da jedes neue Projekt und jeder neue optische Aufbau nun mit der Vorhersage, Suche und Messung des dritten harmonischen Signals beginnt. Mit meinen Simulationen des nichtlinearen Stroms fünfter Ordnung können wir nun die nichtlineare Reaktion undotierter Proben auf einfallendes Pumplicht modellieren. Die Elektronentemperatur, die bei der Messung scharfer Übergangsresonanzen eine

Schlüsselrolle spielt, ist mit den verfügbaren Simulationen zugänglicher geworden.

Das Verfahren, das ich entwickelt habe, um Geräte für das Graphen-Gating vorzubereiten, ermöglicht es uns, Graphen-Nichtlinearitäten aufgrund ihrer extremen Abstimmbarkeit weit über den Spektralbereich im nahen Infrarot hinaus zu untersuchen. Jetzt können die Proben innerhalb von nur zwei Arbeitstagen in unserem optischen Labor vorbereitet und vollständig charakterisiert werden.

Acknowledgements

Through my internship at the research group of Professor Philip Walther I have received a lot of support and assistance. I would first like to thank Philip for letting me become a part of his group.

I would like to thank all the members of "Team Graphene" for everything they taught me in these years.

A special thanks goes to Lee, who supervised me through my bachelor's and master's projects, answered myriads of questions, and always gave valuable advice. He showed me how the scientific approach works and over the years turned into my role model.

I remember the first day I entered our main office to meet Ira and Lee, knowing only how to solder and beam-walk. Now I can single-handedly manage scientific projects. I greatly appreciate every bit of help I received from people around me.

Most of all, I would like to thank my parents for giving me this opportunity and support.

Contents

Introduction

Graphene was the first 2D-material to be produced, and even with time it has remained the most studied. It has unique electronic properties, that give rise to a range of nonlinear optical responses. The goal of "Team Graphene" is to learn how to exploit these nonlinearities. Since we are relatively new to the field of nonlinear optics, we are still building up the toolkit, and structuring our workflow. My master's project focuses on several fundamental aspects required to start this line of research, from the implementation of theory through computer simulations to the development of a protocol to make our graphene samples.

In some materials, the polarization density responds nonlinearly to the intensity of the impinging light. Such materials can squeeze the volume of an optical mode many orders of magnitude smaller and change its frequency. The order of the nonlinearity n tells us which material constant $\chi^{(n)}$ is used to convert the field of strength $\mathbf{E}^n$ into an electric polarization density $\mathbf{P}$, which is responsible for re-emitting light.

There are several different nonlinear phenomena which can take place, often simultaneously, at each order of nonlinearity. For example, when illuminating a material with a strong $\chi^{(3)}$, we expect three fields to interact and generate a fourth field (four-wave-mixing). Furthermore, the material's refractive index can change from n_0 to $n_0 + n_2\langle\mathbf{E}^2\rangle$ (Kerr effect), and the modified refractive index can then apply phase shifts to the light field (self-phase modulation).

Another effect such a material can produce is third-harmonic generation (THG), in which three photons are absorbed to generate a photon of triple frequency. The converted photons are emitted in both directions along the laser beam, so they can be measured either in transmission or in reflection. THG is arguably the most straightforward third-order nonlinear effect and the easiest to measure. Comparing the strengths of the incoming and outgoing fields one can estimate the material constant $\chi^{(3)}$.

The ability of a material to generate nonlinear signals largely depends on its symmetry properties. Graphene, for example, is centrosymmetric. When looking at its hexagonal unit cell in a coordinate plane placed in the center of the hexagon, one can see, that for every point (x, y) on the unit cell there exists an indistinguishable point $(-x, -y)$. In other words, a centrosymmetric material's unit cell is symmetric over the center of the coordinate plane. In such materials, destructive interference prohibits the generation of even-numbered nonlinear signals. In other words, $\chi^{(n)} = 0$ if n is an even number.

Despite being unable to generate even-ordered nonlinear signals, graphene's odd-ordered nonlinearities turn out to be stronger than any other known two-dimensional material. Due to experimental challenges in detecting the higher-order processes, third-harmonic generation has so far been the most studied effect.

Small generation probabilities, difficulties with filtering light, and requirements of using high-power light sources make high-harmonic generation (HHG) in graphene a harder to achieve, but it is still one of the most desirable nonlinear optical processes. HHG was investigated in atomic gases to reach ultraviolet and soft x-ray spectral regions with attosecond radiation generation (3; 4). It was also observed in crystalline solids and used as a method of describing their electronic properties (5; 6). A high density of atoms and the periodicity of crystal lattices makes the mechanism of HHG in solid bodies fundamentally different from that in atomic gasses. For instance, it was recently shown that the orientation of the electric field relative to the crystal axis

plays a role (6; 7; 8).

HHG generation can be useful in nonlinear optics in many ways: it allows one to probe the symmetry of electronic band structure in crystals (6), study interatomic bonding (7) and investigate Berry curvature of materials (8). It was also recently shown to respond to signals of GHz frequencies (9). This sensitivity of HHG to its surroundings not only makes it a useful tool in solid-state physics but also hinders one from studying this effect in itself. Many different theories describe solid-state HHG, but still, there is not one unified predictive theory.

Attempting to study HHG in crystals might be awkward, because some essential features of the process may be swept away by the propagation effects (phase-matching conditions for example) in the bulk of the crystal. This motivates the research in two-dimensional materials.

When studying the interaction of a material with light, it is of great use if one can actively tune the electro-optical properties of a material. This allows one to best tailor the material system for the interaction with a light field of a particular wavelength. In graphene, this is possible due to its continuous linear band structure. Creating a simple capacitor with graphene being one plate, a conductive material (like silicon) being the other plate, and a dielectric material (such as silicon oxide) separating the two plates, it is possible to actively tune graphene's optical response. Electrostatic doping is more universal than chemical doping (using impurities) because chemical doping is passive. Chemically doped devices have to be produced specifically for their application, whereas electrostatically doped devices, once produced, can be re-used and re-tuned for new laser conditions and new applications.

When electrostatically doping graphene, we change the number of charge carriers in the graphene sheet. Roughly speaking, having more charge carriers makes graphene more "sensitive" to light of certain frequencies. Monitoring the current through the graphene sheet allows us to estimate the currrent doping level and orient ourselves in the electronic band structure. For example, the lowest charge carrier concentration corresponds to the point of maximum resistance in a band; this is known as the charge neutrality point (CNP), or the Dirac Point. Being able to gate the further away from the CNP allows us to make the transition resonant to a given frequency over a very large spectral range.

When light interacts with a material, like graphene, sometimes collective electron field excitations emerge, also known as plasmons (10). They travel through a material like a wave on the water surface, until they dissipate, and re-emit some of the absorbed light. In some material systems, the strength of a nonlinearity largely depends on the plasmon lifetime. Plasmon lifetime can be reduced by impurities, low-quality wrinkled graphene, or scattering with atomic vibrational modes, that exist in solids - phonons. Another important contribution to plasmon dissipation is electron temperature. In experiments conducted at room temperature, even at low laser fluence, plasmons only live several dozens of femtoseconds. However, it has been shown, that cooling down the material to cryogenic temperatures can prolong plasmon lifetimes. In (11) the authors measured plasmon lifetimes at 60 K (which is easily accessible with almost any cryogenic setup) to be 1600 fs. This motivates our further research into using cryogenic temperatures for gatable graphene plasmonics, for which my master's project laid the groundwork, by implementing theory to predict the electron temperature in graphene.

This thesis is an overview of all the projects in which I have participated as a research intern in the group of Professor Philip Walther. In these three years, I learned the basics of research in nonlinear optics. I built experiments, took measurements, and analyzed data together with my

colleagues.

In my masters project I worked on simulations, which will be presented in Chapter 2, and experiments in Chapter 3. Before going into the details of those projects I will present the background required to understand the motivation and significance of my work for setting up a self-sustaining lab studying nonlinear optics.

In particular, my personal contributions include:

- Simulation of the electron temperature in graphene, and its dependence on doping and fluence (Section 2.1).
- Simulation of graphene's third-order nonlinear susceptibility, and its dependence on doping, optical power, and electron temperature (Section 2.2).
- Simulation of graphene's third- and fifth-order nonlinear currents, and its dependence on the ellipticity of impinging light (Section 2.3).
- Setup, optimization, and automation of a Fourier transform spectrometer (Section 3.1).
- Optical measurements of third- and fifth-order nonlinear signals in graphene nanostructures (Section 3.2).
- Establishment of the production of graphene samples for electrostatic doping (Section 3.3).

These projects will be discussed in more detail in the following chapters. The Appendix contains technical details on sample preparation and simulation code.

Chapter 1

Background

1.1 Electrical Properties

To study how graphene interacts with light we need to know its electrical properties. We also need this information to create electro-optical devices by combining graphene with other electric materials.

The band structure of graphene and its relaxation time (carrier mobility) define graphene's electronic structure almost completely.

The characteristic dispersion relation for graphene is:

$$E_{\pm}(\mathbf{q}) \approx \pm v_F |\mathbf{q}| \tag{1.1}$$

with **q** being the electron momentum relative to the Dirac Point (located in **K** or **K'** points of the first Brillouin zone), and the plus and minus signs corresponding to the lower π and upper π^* bands, respectively. The proportionality factor between the electron energy and momentum is the Fermi velocity:

$$v_F = \frac{3ta_0}{2\hbar} \approx c/300 \tag{1.2}$$

where $t = 2.8$ eV is the hopping energy between neighboring electron orbitals and $a_0 = 1.421$Å is the distance between the two neighboring carbon atoms in the lattice.

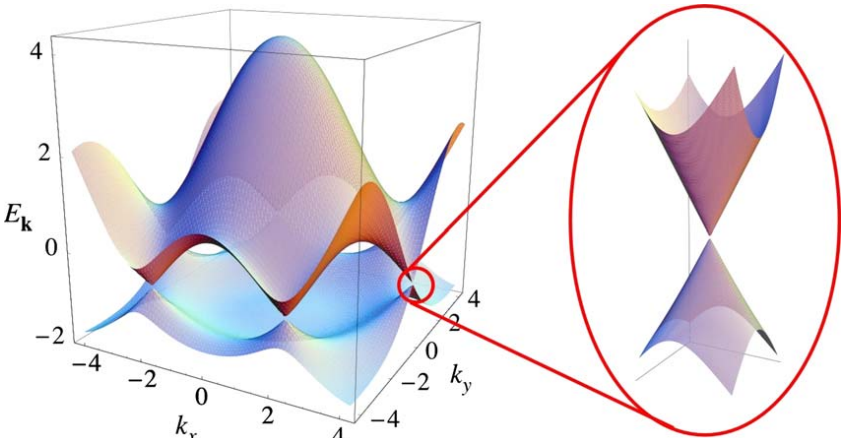

Figure 1.1: The band structure of graphene honeycomb lattice and the Dirac cones. (12)

The constant Fermi velocity is a consequence of the unique band shape (figure 1.1). At the **K** or **K'** points of the first Brillouin zone the bands form symmetric Dirac cones with zero

curvature. This leads to the effective mass of the charge carriers m^* also being zero. This is why charge carriers in graphene exhibit no inertia and drift at a constant speed. The so-called conic approximation is only valid up to a few electronvolts away from the Dirac point (13), which is the region relevant for our project since the light energy used in our experiments is much lower than this threshold.

As the electrons are described by relativistic dynamics, they can be seen as delocalized over the whole graphene sheet. This delocalization is what causes a strong suppression of electron scattering, leading to unusually high electron mobility. In high-quality samples electron mobility could reach up to 10^5 cm^2/Vs (14).

1.2 Optical Properties

The linearity and symmetry of the Dirac cones also leads to an interesting optical feature. When $E_F = 0$ the conduction band is empty. Since there is no band gap, all transitions for electrons from the valence band are allowed, independent of the frequency of the excitation light. This results in a relatively flat absorption spectrum over a wide spectral range (Figure 1.2).

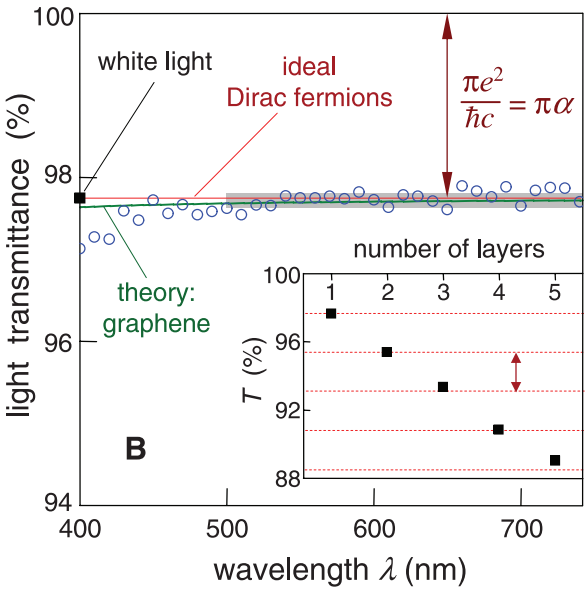

Figure 1.2: Transmittance spectrum of graphene from near-infrared to violet. The vertical red line indicates the opacity.(15)

Thus strong absorbance at visible frequencies enables a unique opportunity to observe the fine structure constant α with a naked eye, as the graphene's opacity is described by:

$$(1 - T) \approx \pi\alpha = 2.3 \pm 0.1\% \tag{1.3}$$

Graphene has a relatively low density of states, thus even weak doping has a large influence on the Fermi energy. This allows for good control over the charge carrier population, which, in turn, influences the optical response.

To understand the optical conductivity of graphene we have to use a modification of the Drude conductivity formula. The Drude model of electrical conduction is used for materials, that show metallic behavior: a sea of jittering electrons and immobile ions. The expression for bulk materials

is:

$$\sigma(\omega) = \frac{ne^2}{m^*}\frac{i}{\omega + i\tau^{-1}}, \tag{1.4}$$

where n is the density of charge carriers, and τ is their scattering time. Getting rid of the scattering time and reducing dimensions we get graphene's Drude conductivity with $\alpha = e^2/4\pi\mathcal{E}_0\hbar c \approx 1/137$ being the fine structure constant:

$$\sigma(\omega) = \frac{ie^2|E_F|}{\pi\hbar^2\omega} = i4\alpha\mathcal{E}_0\frac{|E_F|}{\hbar\omega} \tag{1.5}$$

Equation 1.5 shows how the linear current increases with increasing doping and drops with increasing illumination frequency. This only describes the metallic behavior of graphene, and does not include the contribution from interband transitions (see section 2.2).

1.3 Nonlinear Optics

The optical properties of certain materials can change in the presence of light. This is the subject of study of nonlinear optics. The presentation of nonlinear optics given in this section is based on (10), and all equations come from (10) unless another reference is given.

For fields that are not too large one can describe the nonlinear optical phenomena through a Taylor-series expansion of the dielectric polarization:

$$\mathbf{P}(t) = \mathcal{E}_0(\chi^{(1)}\mathbf{E}(t) + \chi^{(2)}\mathbf{E}^2(t) + \chi^{(3)}\mathbf{E}^3(t) + ...) \tag{1.6}$$

$\chi^{(n)}$ is the nonlinear susceptibility of the material (tensor of rank n+1). To have a term with this factor in the equation means the material has an n-th order nonlinearity. Nonlinear susceptibilities of different order are highly dependent on the symmetry properties of the material. The reason why such phenomena are called nonlinear is that some materials change their optical response in a nonlinear manner. For example, the strength of the optical field created by third-harmonic generation scales cubically with the strength of the input field.

Two systems of units are typically used in nonlinear optics: the Gaussian and the MKS. To avoid confusion and unnecessary conversions we will use the Gaussian system of units (esu) throughout this thesis.

Using the Drude model just like we did to obtain the equation 1.5, we can write down another expression, which will be useful later on:

$$\mathbf{j} = \sigma^{(1)}\mathbf{E} + \sigma^{(2)}\mathbf{E}^2 + \sigma^{(3)}\mathbf{E}^3 + ... \tag{1.7}$$

This is an expression for nonlinear currents $\mathbf{j}$, emerging when a material with nonlinear conductivity σ is illuminated by an electric field of strength $\mathbf{E}$.

Theoretically it is easier to simulate the electric field distribution and obtain expressions for conductivities. Experimentally, one can estimate the nonlinear susceptibility from input and output powers.

1.3.1 Second-Harmonic Generation

As stated above, nonlinear susceptibility is mathematically described as a tensor. The symmetry properties of a particular crystal define the form of linear and nonlinear susceptibilities.

One of the main crystallographic properties of graphene is that it is centrosymmetric (has a center of inversion). For centrosymmetric crystals the second-order nonlinear susceptibility vanishes. This makes it almost impossible to generate second-harmonics, as well as all even-numbered-harmonics.

1.3.2 Third-Order Nonlinearities

Third-order nonlinearities are the most studied nonlinearities in graphene. They are "low-ordered" enough that their generation efficiency is relatively high. This makes the third-order signal relatively detectable and distinguishable in the measured spectrum. Also, for third-order nonlinearities there exist several ways of converting a signal, including:

- Four-wave-mixing
- Optical Kerr effect
- Self-phase modulation
- Two-photon absorption
- Third-Harmonic Generation (THG)

In FWM three fields interact to generate the fourth field. The first field makes the polarization in the dielectric medium oscillate, the second field may interfere with the first creating new fields with sum (or difference) frequencies generation. The third wave will beat with the product of interference creating the fourth field. Since each of the produced beat frequencies can act as a new source field we can use this process to create different types of fields by tuning the input light waves.

The optical Kerr effect describes an additional term that can be generated when describing the refractive index of some materials:

$$n = n_0 + n_2\langle \mathbf{E}^2 \rangle \tag{1.8}$$

where n_0 is the index of refraction one knows from the basics of optics and n_2 is the second-order index of refraction that scales with the strength of the electromagnetic field interacting with the material. The brackets around $\mathbf{E}^2$ represent a time average.

The optical Kerr effect can also cause nonlinear phase shifts, that can be described by

$$\Delta\Phi^{\text{nonlinear}} = \frac{2\pi}{\lambda}\Delta nL = \frac{2\pi}{\lambda}n_2 IL \tag{1.9}$$

where λ is the vacuum wavelength, L is the length of the medium and I is the intensity. The effect where the laser beam changes it's own phase through a nonlinear interaction with a material is called self-phase modulation.

Two-photon absorption may happen when each photon doesn't have enough energy to complete the transition between real energy levels of an atom alone (in this spectral range the material is transparent). They can instead bridge the energy gap by being absorbed simultaneously. When the first photon is absorbed, it makes a virtual transition to a nonexistent level, if the second photon arrives within the virtual lifetime of this state, the transition can be completed. Otherwise the virtual transition collapses to the ground state.

The last process called THG describes the effect when three photons are absorbed to generate one output photon of triple frequency.

There are many different reported values for $\chi^{(3)}$ in the field, and they vary by orders of magnitude. Part of this is likely due to different experimental conditions, such as wavelength, power, or the quality of the graphene samples. The highest values have an order of magnitude 10^{-6} esu.

1.3.3 Fifth-Harmonic Generation

High-harmonic generation (HHG) is an effect of the simultaneous absorption of $n > 3$ photons followed by emission of one frequency converted $(n \cdot \omega)$ photon. It has not been studied as well as THG, because it is less efficient, and experimentally more challenging to measure.

HHG has already been observed at THz frequencies (16), the introduction of a small band gap has been shown to increase the optical response (17; 18). It was also shown to be polarization dependent in the mid-infrared in different ways at high (19) and low light intensities (20). At high intensities the nonlinear current shows a peak at finite ellipticity at low intensities the nonlinear current monotonically drops as ellipticity increases.

The 5th-order signal (as well as the 3rd-order) experiences blue shifts, that scale inversely with pulse duration (20). The blue shift also depends on ellipticity, being maximal for linear fields and minimal for circularly polarized light. This effect can be explained either by the quantum dynamics of charge carriers or by the effect of vanishing THG under circularly polarized illumination due to the crystal symmetry (21). Furthermore, the induced blue shift is an interband effect.

When measuring the HHG filtering becomes one of the most significant experimental challenge. Higher-order signals have generation probabilities orders of magnitude lower than third-order signals. This leads to very low photon counts, compared not only to the simultaneously occurring THG processes, but also to the optical background noise of the measurement setup. Apart from using spectral filters we used spectroscopic techniques to enable us to distinguish different spectral features, and Pauli blocking can be used to suppress lower energy transitions using electrostatic gating.

Chapter 2

Simulations

The first part of my contribution to the research of "Team Graphene" that I will present are simulations that I did for comparison to experimental data. In this chapter, the theoretical approach to graphene nonlinearities is described. The simulation code I wrote can be found in Appendix.

2.1 Electron Temperature

My simulations were based on the results of (22). Hence, all of the equations presented in this chapter where taken from (22).

When simulating $\chi^{(3)}$, the electron temperature plays a significant role. As discussed in (23) the photo-excited electrons can thermalize within a few tens of femtoseconds. This can lead to electron temperatures much higher than ambient temperature. Generally, one-photon interband transitions are responsible for turning absorbed light into electron temperature. We can then distinguish two cases:

- $E_F < \hbar\omega_0$ one-photon transitions are allowed and T_e can reach a few thousand degrees.
- $E_F > \hbar\omega_0$ one-photon transitions are suppressed and T_e stays close to ambient temperature.

To have a model for electron temperature we have to assume a fraction γ of the incident photon energy absorbed by the hot electron distribution. We can retrieve an exact value of γ by measuring the normalized $\frac{\mathsf{T}(V_g)}{\mathsf{T}(V_{\mathsf{CNP}})}$ transmittance spectra and fitting the fluence dependence by a power law at high fluence limit, which scales as $F^{1/3}$ in charge neutral and as $F^{1/2}$ in highly doped graphene. In our experiment (24) the fitted value for γ was set to 3.5×10^{-3}, consistent with the previously reported value of 1.7×10^{-3} (22). The experimental results will be discussed in section 3.2.

To calculate the temperature of hot electrons we use the heat capacities $C_e = \beta T_e^2$ for undoped graphene, and $C_e = \alpha T_e$ for highly doped graphene.

Important factors are

$$\beta = \frac{18}{\pi}\frac{\zeta(3)}{(\hbar v_f)^2}k^3 \tag{2.1}$$

and

$$\alpha = \frac{2\pi}{3}\frac{eE_F}{(\hbar v_f)^2}k^2 \tag{2.2}$$

Where k is the Boltzmann constant, and ζ is the Riemann zeta function

$$\zeta(s) = \sum_{n=1}^{\infty} n^{-s}$$

In our case $\zeta(3) = 1.202$.
Using the equations above we get the formula for hot electron temperature in undoped graphene:

$$T_e^{\text{CNP}} = T_0 \left(1 + \frac{3\gamma F}{\beta T_0^3}\right)^{\frac{1}{3}} \tag{2.3}$$

And in highly doped graphene:

$$T_e^{\text{doped}} = T_0 \left(1 + \frac{2\gamma F}{\alpha T_0^2}\right)^{\frac{1}{2}} \tag{2.4}$$

Where $T_0 = 300$ K is ambient temperature. Using parameters of our laser system such as average power $P = 5.2$ mW, repetition rate $f = 80$ MHz, and spot size of $d = 20$ μm we use $F = (P/f)/d$ to get laser fluence of 20.6 μJ/cm^2.

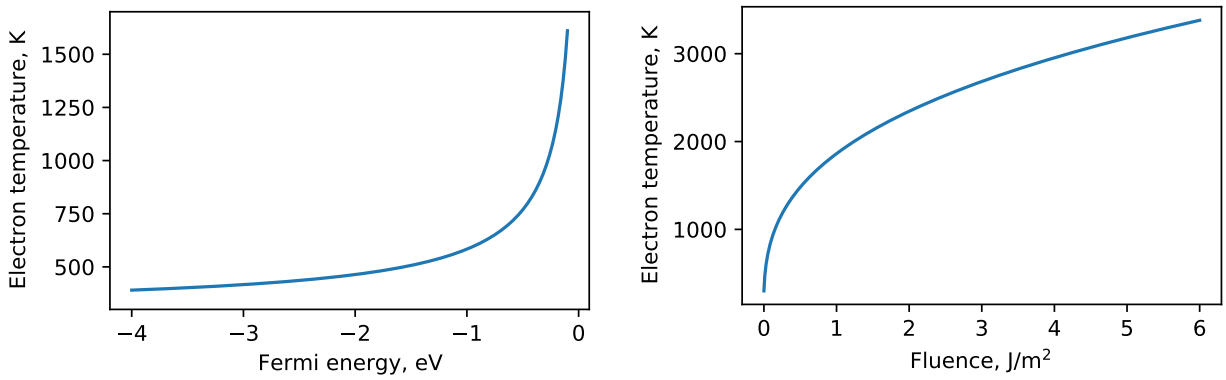

Figure 2.1: Electron temperature of heavily doped (up to -4 eV) and undoped (right) graphene. For heavily doped graphene the fluence $F = 20$ μJ/cm^2 was used.

Combining both curves into one helps us find the transition point. In a typical optical experiment, the laser fluence is kept constant while the Fermi energy of graphene is tuned. Thus we are interested in T_e versus E_F for a fixed fluence.

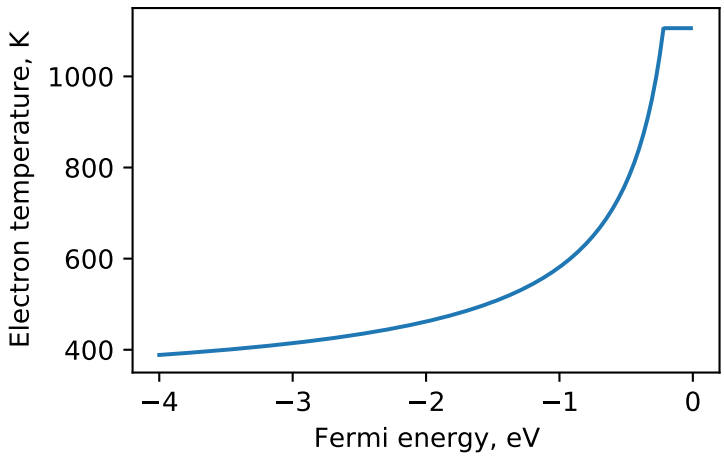

Figure 2.2: Transition curve between undoped and doped regimes.

The transition point is clearly visible in the figure 2.2 at a doping of -0.22 eV for ($\lambda_0 \approx 5.5$ μm). Here we assume a smooth transition from the undoped state with the electron temperature residing at a constant maximum of 1100 K until the doping reaches the transition point. Then the electron temperature rapidly decreases as described by equations 2.2 and 2.4. The strongest doping our samples can reach is around 1 eV (more on this in section 3.3.2). At this level the electron temperature drops to about 580 K - the "coldest" we can get without using the cryostat.

Note: this curve is more a visualization, than an exact description. The behavior of electron temperature in the transition zone is yet to be described theoretically. Intuitively, it is expected to be a sigmoid function like in figure S6b in Supplementary Material of (25).

2.2 Chemical potential

To make a nonlinear signal more pronounced we can attempt to tune optical transitions into resonance with our pump laser.

There are two types of optical transitions in crystalline solids, whose electronic structure is described by the band theory. These two are intraband and interband transitions (figure 2.3).

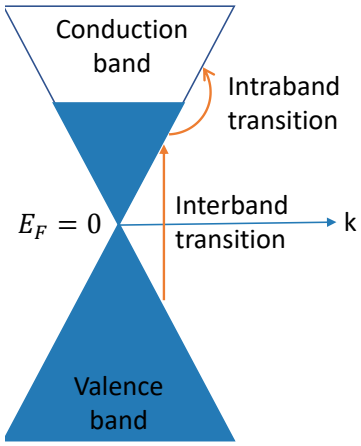

Figure 2.3: Intraband and interband transitions on a continuous Dirac cone.

As discussed in section 1.1, using the tight binding model we obtained the Dirac cones as an approximate solution to the Schrödinger equation. However, this solution is only true if we assume of a system of infinite size, perfectly flat and without perturbations. If the system has special geometry, is doped or under external fields, it has to be described taking into account boundary conditions. As a result, the Schrödinger equation has quantized solutions. This creates bands inside the cone. Now the system is not linear anymore and one speaks of intraband transitions as transitions inside of the band and interband transitions as transitions between the bands, where the excitation energy should match the energy needed for the transition.

Adding new charge carriers to the system without creating disorder means changing the chemical potential relative to the charge neutrality point ($E_F = 0$). For simplicity we will discuss a system at T=0 with a continuous Dirac cone. Due to it's symmetry, increasing the amount of electrons gives an increase in the amount of holes, thus changing the chemical potential by an amount μ shifts the Fermi level by $2|\mu|$.

As discussed above, the higher the chemical potential the more single-particle states are filled.

Thus more states are prohibited from being excited by optical transitions. We can tune the chemical potential to prohibit some transitions that take away from THG or HHG. We can also set the Fermi energy to be resonant to chosen multiphoton interband transitions.

As described by (26) each transition has its own resonance in the $\chi^{(3)}$ describing THG:

$$\chi^{(3)}_{xxxx} \propto \left[-17G\left(\frac{\hbar\omega_0}{2|\mu|}\right) + 64G\left(\frac{2\hbar\omega_0}{2|\mu|}\right) - 45G\left(\frac{3\hbar\omega_0}{2|\mu|}\right)\right] \tag{2.5}$$

with $G(x) = \ln\left|\frac{1+x}{1-x}\right| + i\pi\theta(|x|-1)$, $\theta(x)$ being the Heaviside step function. The first term corresponds to the one-photon transition, the second term to the two-photon transition, and the third term to the three-photon transition. Notice also that the terms contribute with different signs.

These G terms describe how the resonant transitions change with chemical potential (visualized in figure 2.4):

- For $2|\mu| > 3\hbar\omega_0$ all resonant transitions are blocked. In this case only nonresonant intraband contributions are left.
- For $2\hbar\omega_0 < 2|\mu| < 3\hbar\omega_0$ both one- and -two photon resonant transitions are blocked. This gives the highest value for $\chi^{(3)}_{xxxx}$.
- For $\hbar\omega_0 < 2|\mu| < 2\hbar\omega_0$ one-photon resonant transition is blocked. $\chi^{(3)}_{xxxx}$ drops.
- Finally for $2|\mu| < \hbar\omega_0$ all terms can contribute, but $\chi^{(3)}_{xxxx}$ is very small. In this case three terms nearly cancel each other out.

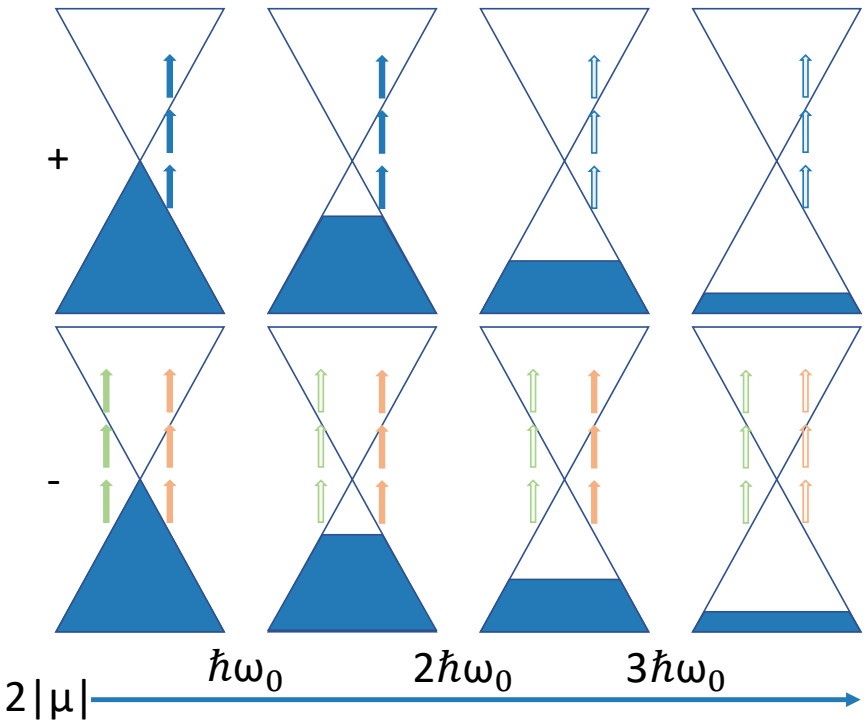

Figure 2.4: One-photon (green), two-photon (blue) and three-photon (orange) interband transitions damped (reduction in brightness) by tuning chemical potential.

However, this picture does not include resonant damping and finite electron temperature effects. If we were to plot this function without damping at T=0 we would observe singularities at $\hbar\omega_0$, $2\hbar\omega_0$, and $3\hbar\omega_0$.

In fact these singularities haven't yet been observed experimentally. One of the current research projects of "Team Graphene" is to observe these sharp peaks at the transition resonances by the use of cryogenic temperatures.

For the experiment mentioned in the previous section, we assumed equal resonant damping factors for interband and intraband resonances. The values were calculated from simulated plasmon lifetimes of $\tau = 25$ fs, which converts into damping energy of $\frac{\hbar}{\tau}$.

We start with the equation describing the third-order conductivity around the Dirac point (eq. 22 from (27)). This equation does not include damping factors and temperature dependence.

$$\sigma^{(3);xxxx} = \frac{i\sigma_0(\hbar v_F e)^2}{48\pi(\hbar\omega)^4} T\Big(\frac{\hbar\omega}{2\,|\mu|}\Big) \tag{2.6}$$

with $T(x) = 17G(x) - 64G(2x) + 45G(3x)$ and $G(x) = \ln\left|\frac{1+x}{1-x}\right| + i\pi\theta(|x|-1)$, $\theta(x)$ being the Heaviside step function.

Using (eq. 1 from (27))

$$\chi^{(3)} = \frac{\sigma^{(3);xxxx}}{-i\omega_t v_0 d_{gr}} \tag{2.7}$$

we can simulate the dependence of the undamped $\chi^{(3)}$ at zero temperature on μ, which is displayed in figure 4b in (25). These resonances will later become smooth, when we include damping.

We then reproduce the results of (26) to include resonant damping in nonlinear conductivity terms. The nonlinear conductivities are described by equations 51 and 52 in (26).

$$\sigma^{(3);xxyy}(\omega,\omega,\omega) = \sigma_A^{(3);xxyy}(\omega) + \sigma_B^{(3);xxyy}(\omega) + \sigma_C^{(3);xxyy}(\omega) \tag{2.8}$$

$$\sigma_A^{(3);xxyy}(\omega) = \frac{i\sigma_3}{144(\hbar\omega)^4}[17G_\mu(\hbar\omega + i\Gamma_e) - 64G_\mu(2\hbar\omega + i\Gamma_e) + 45G_\mu(3\hbar\omega + i\Gamma_e)] \tag{2.9}$$

$$\sigma_B^{(3);xxyy}(\omega) = \frac{\Gamma_i\sigma_3}{\hbar 36(\hbar\omega)^4}[-8H_\mu(2\hbar\omega + i\Gamma_e) + 17H_\mu(3\hbar\omega + i\Gamma_e) + 3\hbar_\mu(3\hbar\omega + i\Gamma_e)] \tag{2.10}$$

$$\sigma_C^{(3);xxyy}(\omega) = -(\Gamma_i - \Gamma_e)^2 \frac{2i\sigma_3}{27(\hbar\omega)^5\,|\mu|} \tag{2.11}$$

The functions used to calculate conductivities are:

$$G_\mu(\nu) = \ln\left|\frac{2\,|\mu| + \nu}{2\,|\mu| - \nu}\right| = i(\pi + \arctan\frac{\nu_r - 2\,|\mu|}{\nu_i} - \arctan\frac{\nu_r + 2\,|\mu|}{\nu_i}), \tag{2.12}$$

where ν_r and ν_i are real and imaginary part of $\nu = \hbar\omega + i\Gamma_e$, respectively, and

$$H_\mu(\nu) = \frac{1}{2\,|\mu| - \nu} + \frac{1}{2\,|\mu| + \nu}, \tag{2.13}$$

$$I_\mu(\nu) = \frac{1}{(2\,|\mu| + \nu)^2} - \frac{1}{(2\,|\mu| - \nu)^2}. \tag{2.14}$$

Plotting these equations results in red curves of figure 3 in (26), which correspond to nonlinear conductivities at 0 K in units of σ_0.

To include temperature effects one has to modify equations 2.12, 2.13, 2.14 using

$$\bar{G}_{\mu;T}(\nu) = \beta \int_{-\infty}^{\infty} dx F_\mu(x,T)[1 - F_\mu(x,T)]G_x(\nu) \tag{2.15}$$

with $F_x = [1 + e^{\beta(x-\mu)}]^{-1}$. Equations 2.13 and 2.14 are modified the same way. To calculate these integrals we replace all μ with x (except the one in F_μ) and use a loop to calculate the value of the integral for every value of ν.

This results in figure 10 in (26) . Using these modified functions to calculate conductivities results in blue curves of figure 3 in (26). Using the values for damping factors and photon energy we obtain figure 4c in (25) (Γ_e now also depends on x).

Figure 2.5(a-c) shows the same function plotted for our experimental conditions. In particular for different electron temperatures and pump energies, as well as the measured Fermi energies that gave largest third-ordered susceptibilities. There is a definite peak as described by the equation 2.5. However, for higher electron temperatures the peak is broadened. This is especially evident for lower pump energies close to $E_0 = 0.225$ eV (darker green curves) corresponding to $\lambda = 5.5$ μm. These pump energies are closest to resonance with the Fermi energy we could reach by gating our samples.

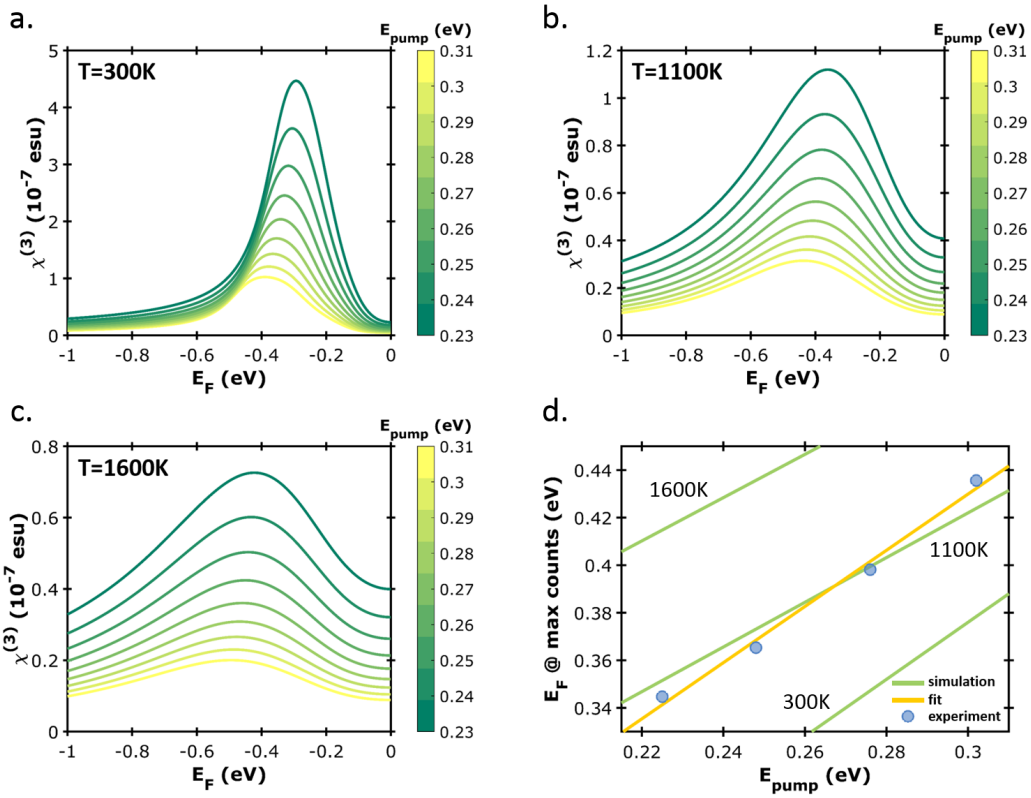

Figure 2.5: a-c. Third-order nonlinear susceptibility as a function of Fermi energy for wavelengths of 4.1-5.5 μm at different electron temperatures. d. Fermi energies for which the maximum third-order susceptibilities were found in the gate measurement shift linearly with pump energy.

2.3 Ellipticity

Apart from all material properties, nonlinear harmonic signals may also depend on the polarization of the impinging light. When taking measurements of fifth-harmonic for our experimental results published in (24) we observed artifacts, that we couldn't explain. Also, there is no theory for the dependence of the fifth-order nonlinear conductivity on chemical potential, and no good explanation for why the optimal gap width in our nanoribbon experiment (figure 3.4 c) is different for third- and fifth-harmonics. This simulation was an attempt to find reasons for the systematic deviation from predicted behavior of our samples. We also plan to make more ellipticity dependence measurements in our future projects, but these are outside the scope of my thesis.

There are at least two different theoretical approaches describing ellipticity dependence of nonlinear signals in the literature (19; 20).

In (19), the authors provide a fully quantum mechanical theory with three different regimes depending on the ratio between the band gap energy and the Rabi frequency. In the semimetallic region ($E_g/2\hbar \leq \Omega_R$), which describes the case for monolayer graphene, they found that HHG yields a maximum at finite ellipticity. However, we decided not to apply this theory to our case, since they use ultrahigh peak fluence (1.7 TW/cm^2) and short pulse duration (25 fs) in their measurements.

In (20), the authors provide another description, which is quite different from the one summarized above due to lower intensities of irradiation. Unlike in (19), a continuous decrease in nonlinear current with polarization ranging from linear ($\varepsilon = 0$) to circular ($\varepsilon = 1$) was predicted and measured. The measurements were performed with a peak fluence of 5 GW/cm^2 and 70 fs pulse duration.

Their theory is accurate in the regime where light intensity is low enough to displace the Dirac cone up to the resonant electron wavenumber $k = \omega/(2v_F)$. The condition is $I \ll 137\hbar\pi^3c^4/2v_F^2\lambda^4$ $\approx$ 200 MW/cm^2 at $\lambda = 5.5$ μm, which is safely met in our experiment with 80 MW/cm^2 peak fluence.

The simulation is based on the equations provided in the supplementary material for (20).

Our goal is to calculate the third- and fifth-order nonlinear current described by equations:

$$\mathbf{J}_{3\omega}(t) = \mathrm{Re}\left\{ \left[\int (\cos\phi\hat{\mathbf{y}} - \sin\phi\hat{\mathbf{x}})(\eta_{\mathbf{k}}^*)^3 f(|\eta_{\mathbf{k}}^*|^2) d\phi \right] e^{-3i\omega t} \right\} \tag{2.16}$$

$$\mathbf{J}_{5\omega}(t) = Re\left\{ \left[\int (\cos\phi\hat{\mathbf{y}} - \sin\phi\hat{\mathbf{x}})(\eta_{\mathbf{k}}^*)^5 g(|\eta_{\mathbf{k}}^*|^2) d\phi \right] e^{-5i\omega t} \right\} \tag{2.17}$$

where f and g are involved functions of $|\eta_{\mathbf{k}}^*|^2$, and $\eta_{\mathbf{k}} = \sin\phi - \cos\phi e^{i\vartheta}$.
We define functions f and g as

$$f = \frac{\hbar k}{eE_0}\xi_3(\eta_{\mathbf{k}} n_{\mathbf{k}}^{(4)} - \eta_{\mathbf{k}}^* n_{\mathbf{k}}^{(2)}) \tag{2.18}$$

$$g = \frac{\hbar k}{eE_0}\xi_5(\eta_{\mathbf{k}} n_{\mathbf{k}}^{(6)} - \eta_{\mathbf{k}}^* n_{\mathbf{k}}^{(4)}) \tag{2.19}$$

Then we use the explicit form of $n_{\mathbf{k}}^{(0)}$, $n_{\mathbf{k}}^{(2)}$, $n_{\mathbf{k}}^{(4)}$ and $n_{\mathbf{k}}^{(6)}$:

$$n_{\mathbf{k}}^{(0)} = -\gamma \left\{ (\gamma - \mathrm{Re}\left[2|\eta_{\mathbf{k}}^*|^2 \xi_1 + \frac{2|\eta_{\mathbf{k}}|^4 \xi_1^2 \beta}{\alpha\beta - |\eta_{\mathbf{k}}|^4 \xi_3^2 \delta} \right] \right\}^{-1} \tag{2.20}$$

$$n_{\mathbf{k}}^{(2)} = \frac{-2(\eta_{\mathbf{k}}^*)^2 \xi_1 \beta}{\alpha\beta - |\eta_{\mathbf{k}}|^4 \xi_3^2 \delta} n_{\mathbf{k}}^{(0)} \tag{2.21}$$

$$n_{\mathbf{k}}^{(4)} = -\frac{1}{\beta} (\eta_{\mathbf{k}}^*)^2 \xi_3 \delta n_{\mathbf{k}}^{(2)} \tag{2.22}$$

$$n_{\mathbf{k}}^{(6)} = \frac{1}{\delta} |\eta_{\mathbf{k}}^*|^2 \xi_5 n_{\mathbf{k}}^{(4)} \tag{2.23}$$

With
$\delta = |\eta_{\mathbf{k}}|^2 \xi_5 - \gamma + 6i\omega$,
$\alpha = \gamma - 2i\omega - |\eta_{\mathbf{k}}|^2 (\xi_1 + \xi_3)$,
$\beta = (\gamma - 4i\omega - |\eta_{\mathbf{k}}|^2 (\xi_3 + \xi_5))\delta + |\eta_{\mathbf{k}}|^4 \xi_5^2)$.
γ being the damping parameter. It describes damping by scattering from impurities and coupling to phonons.

We define two cases: linear ($\vartheta = 0$) and circularly ($\vartheta = \pm\pi/2$) polarized light. In the first case $|\eta_{\mathbf{k}}|^2$ depends on ϕ which gives us a description for nonlinear currents, in the second $|\eta_{\mathbf{k}}|^2 = 1$ and thus shows no dependence on ϕ.

The equations 2.16 and 2.17 are then reduced to

$$\mathbf{J}_{3\omega}(t) = \mathrm{Re}\left\{ \pm i \left[\int (\sin\phi \hat{\mathbf{x}} - \cos\phi \hat{\mathbf{y}}) e^{\mp 3i\phi} d\phi \right] f(1) e^{-3i\omega t} \right\} = 0 \tag{2.24}$$

and

$$\mathbf{J}_{5\omega}(t) = \mathrm{Re}\left\{ \pm i \left[\int (\cos\phi \hat{\mathbf{y}} - \sin\phi \hat{\mathbf{x}}) e^{\mp 5i\phi} d\phi \right] g(1) e^{-5i\omega t} \right\} = 0 \tag{2.25}$$

To evaluate the integral we run the values of ϑ from 0 to $\pi/2$ and integrate over ϕ from 0 to 2π. The resulting integral is then plotted versus ϑ.

Figure 2.6 shows a decrease in the nonlinear current generation with increasing ellipticity of illumination. For predicting the reduced optical response it is sufficient to calculate the normalized currents since the expected drop in the conductivity is also known using the Drude conductivity formula: $J = \sigma \cdot E$.

The polarization angle ϑ goes from 0 to 2π, showing a gradual change from linearly polarized light to circularly polarized, and back to linear. The fifth-order current shows a much stronger dependence on ellipticity, than the third-order current, which is what the authors of the "finite ellipticity" paper also predict for the semimetal regime in their theoretical description (28).

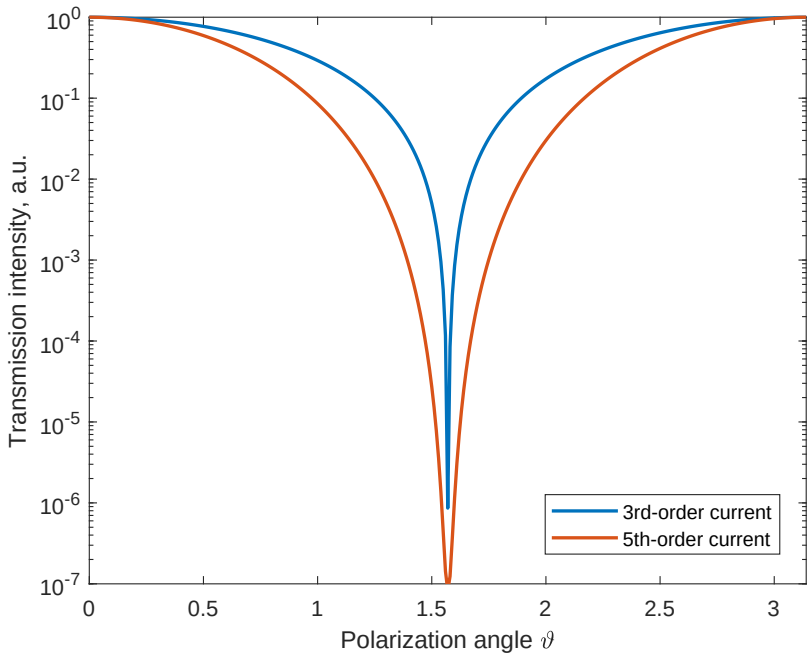

Figure 2.6: Transmitted third- and fifth-harmonic intensity as a function of polarization angle.

The above curve was experimentally proven to be correct in (20). The resulting third harmonic signal was shown to drop by two orders of magnitude with growing ellipticity, compared to linearly polarized light. The authors attribute this reduction to the trajectories of field-driven electrons in the k-space. Also, this behavior is not unique to graphene, since it partly has to do with the symmetry properties of the crystal. In (21) the authors say, that three-fold rotational symmetry, which is also present in graphene, forbids THG with circularly polarized light.

The behavior simulated in this section is useful for polarization dependence measurements. These measurements are often performed in nanostructured samples if the dependence of signal generation on nanostructure spatial orientation has to be shown as we do in (24).

Chapter 3

Experiments

In this chapter, I will discuss the various experiments, in which I participated these past years.

I started by learning the basics of experiments in nonlinear optics when working on the nanostructured graphene experiment, discussed in section 3.2. My contribution was the characterization of optical elements used in the experiment, as well as the optimization of the optical setup. During that time we had collaborators from ICFO send us samples, which we would analyze with our optical setup. After the collaboration was over, we started looking for ways to make samples ourselves. This became the main part of my master's project. Section 3.3 describes the lessons we learned, and the progress we made. The chapter begins, however, with a description of a smaller project - the Fourier transform spectrometer I made for the fast acquisition of absorption spectra.

3.1 Spectroscopy

Another contribution to the research of "Team Graphene" that I've made was building an FTIR Spectrometer for fast device characterization. Since we don't have our own FTIR spectrometer, we have to borrow devices from other research groups. Normally it takes us a day to make a spectral measurement, and we must schedule time in advance. With the device described here, we can take measurements over a micron of spectral range with several nanometer spectral resolution in 15 minutes using a basic oscilloscope found in our lab. Using a USB-oscilloscope, the measurement times could be reduced tenfold. Also, software for device control and measurement automatization was written.

The reason for building such a setup comes from the recent interest in electronic and optoelectronic applications of single-wall carbon nanotubes (SWNTs). Particularly, the reported value of $n_2 \approx 2.2 \times 10^{-8}$ esu for the nonlinear refractive index measured at telecom wavelength using the four-wave mixing technique (29). The authors measured the transmittance spectrum of the device in the infrared for device characterization, which showed a clear dip around the wavelength of the resonant transition. The value for n_2 lies close to the ones previously reported for graphene, which makes SWNT-based devices worth further investigation for nonlinear optics.

Our FTIR spectrometer is based on a commercially available interferometer called the GEMINI. More on it in the following section.

3.1.1 GEMINI Interferometer

The GEMINI (also referred to as Translating-Wedge-based Identical pulses eNcoding System) is a time-delay interferometer. The original version of the GEMINI consists of two polarizers and two birefringent optical elements (blocks A and B in figure 3.1). Its mirrors don't move, only one wedge of block B moves. The optical axis of the birefringent element is the extraordinary axis, and it has to be perpendicular to the propagation direction, otherwise it won't cause a phase shift.

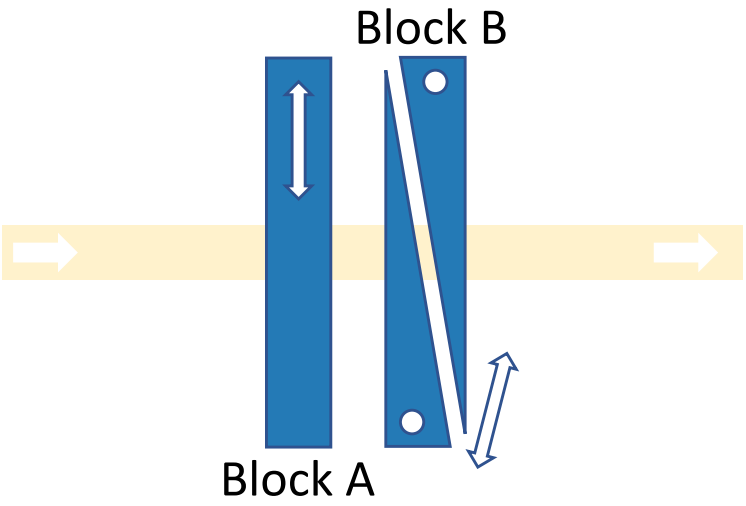

Figure 3.1: Simplified scheme of the GEMINI interferometer.

The first input polarizer (45° to the optical axis of birefringent elements) splits light in two orthogonal polarizations. Block A introduces a relative phase shift on one of the polarizations using its birefringence $\Delta n = n_e - n_o$:

$$\tau = \Delta n \frac{L}{c} \tag{3.1}$$

Block B compensates for this phase shift. One of the wedges of block B is mounted on a precision linear positioner (wedge insertion x), to create an angle $\pi/2 - \alpha$ with respect to the light beam, maintaining the distance between the two wedges constant. It allows for control of τ with attosecond precision:

$$\tau(\nu, x) = \Delta n(\nu) \cdot x \cdot \sin \alpha / c \tag{3.2}$$

where α is the apex angle between the wedges of block B.

By moving the wedge of block B we vary the thickness of the block, deciding how much we want to compensate for the phase shift. The distance between wedges is kept constant. The principle is the same as if we used 2 waveplates, but much more stable and precise. The same system could also be made using only block B, but using both gives more tunability. We can tune translation with more precision, than rotation.

The output polarizer can be oriented either orthogonally or parallel to the input polarizer, depending on which beam one chooses to measure: the reflected or the transmitted output beam of the interferometer.

Both replicas share the same channel inside the GEMINI, so noise is also correlated for both replicas. Also, one doesn't have to take care of the spatial overlap, like in a Michelson interferometer, where we would have to overlap beams perfectly for interference. Having moving mirrors means no alignment to take care of. In a Michelson interferometer, moving a wedge by a distance x changes the path length by $2x$. In the GEMINI it's $\Delta n \cdot \sin \alpha \cdot x$, which leads to the positioning error of the GEMINI being two orders of magnitude smaller than that of Michelson's interferometer.

The main advantage, however, is that, in contrast to an ordinary Michelson interferometer, the GEMINI's time delay τ is wavelength dependent, due to its birefringency $\Delta n(\nu)$. Therefore, one obtains a recorded interferogram as a function of x:

$$I(\tau) = \int |E(\nu) + E(\nu)e^{-2i\pi\tau(\nu,x)\nu}|^2 d\nu = \int |E(\nu) + E(\nu)e^{-2i\pi\frac{\Delta(\nu)\cdot\sin\alpha\cdot x}{c}\nu}|^2 d\nu \tag{3.3}$$

The GEMINI works in the visible, IR and UV spectral ranges.

3.1.2 FTIR Spectrometer

The setup I built for characterizing the samples is schematically shown in figure 3.2. It consists of a power-stabilized Tungsten broadband infrared lamp, lenses to focus light on the sample and reduce the beam diameter, the GEMINI interferometer is surrounded by two polarizers, an optical chopper and a photodetector. The optical chopper wheel, which is a rotating disc with mechanical shutters, was used to make a lock-in measurement by intensity-modulating the signal, while keeping the background noise constant. Since the light source is incoherent the most challenging alignment was to collimate the beam well enough that it could pass through the interferometer without losing too much power. The spectrometer currently operates in the range 1-5 μm. It can be further extended to the visible spectral range by changing the detector, both polarizers and re-calibrating the interferometer. Examples of spectral measurements taken with this setup can be found in figure 3.3.

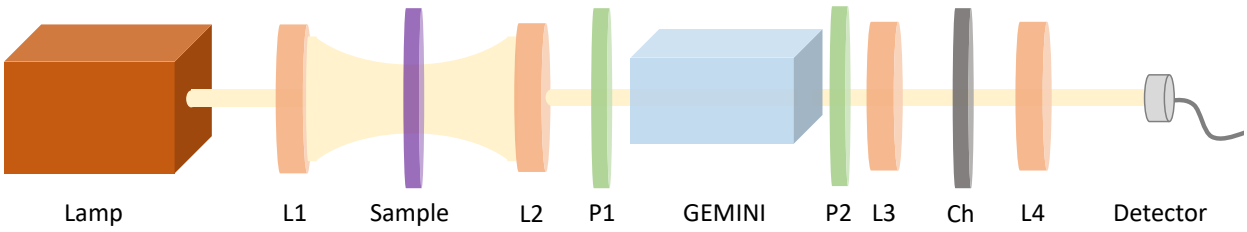

Figure 3.2: FTIR Spectrometer

The setup was built using an infrared lamp (Thorlabs SLS202: 450 - 5500 nm) and a PbSe transimpedance amplified photodetector (1.5-4.8 μm). The detector has AC coupled amplifiers, so it requires an optical chopper and an oscilloscope to measure the output voltage. We used Thorlabs MC2000B optical chopper with MC1F30 Blade (60-3000 Hz) and a Rohde Schwarz HMO 3004 oscilloscope. The chopper is set at 3000 Hz for higher precision of voltage measurements.

Our FTIR Spectrometer works the following way:

- Measurement parameters are fed into the Spectroscopy widget of Graphene Lab GUI.
- GEMINI finds its start and end points and begins the scan.
- At each step of the GEMINI scan an electric waveform is acquired by the oscilloscope. The waveform is then converted to V_{RMS} and split in 10 fragments. Each fragment is windowed and fast-Fourier-transformed. The resulting electric spectra are then averaged, peaks above the power threshold are evaluated. The peak with the highest voltage becomes the measurement output at the first step of the GEMINI scan.
- The measured voltages are plotted real time in the interferogram.
- At the end of the measurement the interferogram is Fourier transformed and becomes the output spectrum.

To test if the setup is working properly we measured spectra of two bandpass filters from Thorlabs: FB1550-12 and FB1750-500. The measured spectra are provided in figure 3.3. The spectra were not averaged, both were acquired with 10 nm resolution at central wavelength. Also, they were not normalized yet, since we are yet to make a better quality measurement of the lamp's spectrum. However, it's worth noting, that artifacts in the spectrum of the second filter are due to the features of the lamp.

Comparing the spectra, we see, that the central peak of the narrow bandpass filter FB1550-12 was measured precisely (figure 3.3 a, c), as well as the locations of the of the edges of the FB1750-500 bandpass filter match the expectation (figure 3.3 d, f). Having precise values for wavelengths is important for us since in the SWNT samples they tell us where the resonant transition is located in the transmittance spectrum.

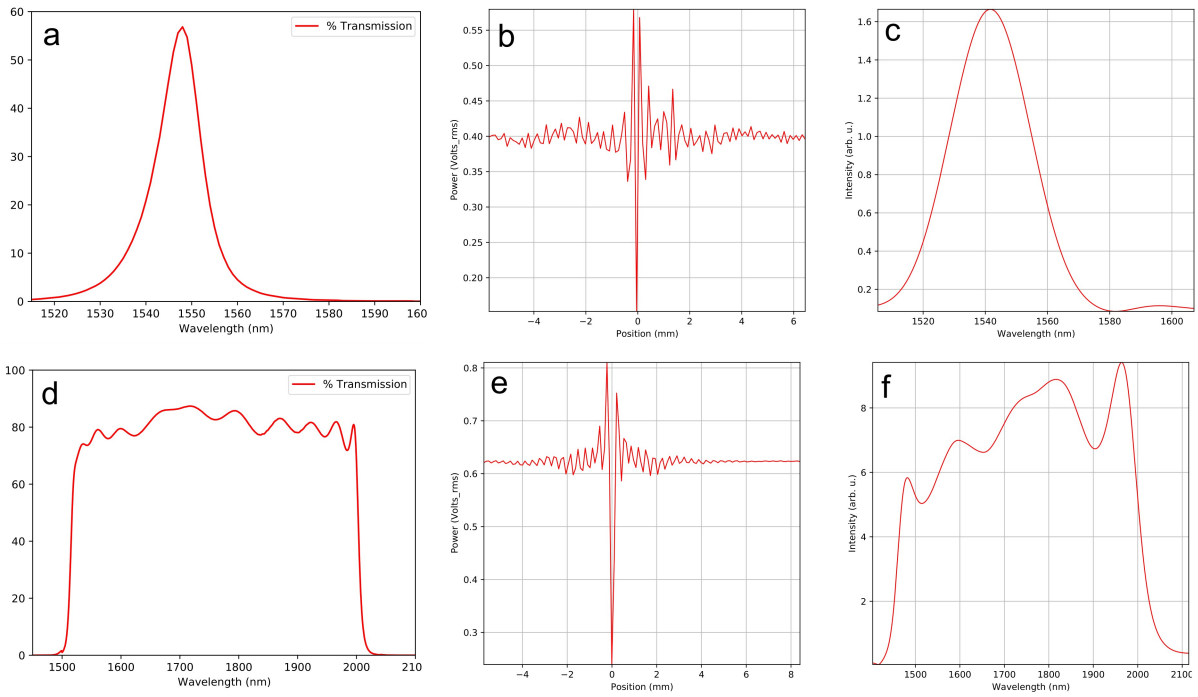

Figure 3.3: Spectra of bandpass filters. a, d Spectra provided by Thorlabs; b, e measurement interferograms; c, f measured spectra. Note: measured spectra are not normalized.

3.2 Heterostructures

One of the projects where I participated investigated nonlinearities in graphene heterostructures. I helped with measurements and the characterization of optical devices used in the experiment described below. I also provided simulations for the evaluation of experimental data described in the previous chapter. Because of these contributions, I became a co-author of the paper.

A crystal, created by elements, forming covalent bonds, can often be separated into atomically thin layers to become, what is called, a topological material. Such materials have strong bonds in the layer and weak bonds between the layers. Isolated atomic planes can be reassembled into heterostructures layer-by-layer in a precisely chosen sequence. These atomic layers are held together only by van der Waals forces. Van der Waals bonds are weak short-range bonds, scaling as $\propto 1/R^6$ in bond energy. This allows for the creation of a "2D Legoland" with heterostructures made of monolayer materials, tailored in their electronic properties (30).

The device analyzed (figure 3.4 a) is a van der Waals heterostructure (31). It consists of a $SiO_2/Si/SiO_2$ substrate, CVD monolayer graphene, Al_2O_3 spacer and gold nanoribbons with different ratios of gold-to-gap width (figure 3.4 c). A gate voltage can be applied between Si and graphene to control the Fermi energy of the latter. In these devices gold nanoribbons intensify the electric field of the incident light, they also improve light coupling into graphene, which helps more efficiently launch graphene surface plasmons. The strongest concentration of the electric field was shown by simulations in the case when the light was linearly polarized perpendicular to the orientation of the nanoribbons. Light is concentrated in the gap ($\approx$ 50 nm size) between the nanoribbons. The width of the nanoribbon and the size of the gap define the resonant wavelength for optimal in-plane plasmon confinement, whereas the spacer thickness defines the out-of-plane confinement.

The sample was analyzed (figure 3.4 d) using a tunable (1-10μm) pulsed laser system (pump, Optical Parametric Oscillator , Difference Frequency Generator) with pulse duration of 260 fs and a repetition rate of 76.2 MHz. Polarizers and band-pass filters were used to filter out light, that was not converted by the DFG. A half-wave plate was used to rotate the beam polarization, so that it matches the orientation of nanoribbons for maximum absorption in the sample. A beam with a wavelength of 5500 nm was focused using a 20 mm aspheric lens, resulting in a beam waist of 20 μm. A sample was mounted on a motorized translation stage and moved in and out of the focus, another band-pass filter was used to filter out unconverted light. The THG output was coupled into a multi-mode optical fiber and measured by a SNSPD (more in 3.2.1). The estimation of values of $\chi^{(3)}$ for planar graphene and nanostructures was done analogously to (25).

The third-order nonlinear optical polarization induced in a graphene monolayer of thickness d_{gr} is given by

$$P^{(3)}(\omega) = \chi^{(3)} d_{gr} E_{in}^3 \tag{3.4}$$

and the output field generated by the polarization is

$$E_{out} = \frac{\alpha}{4} \frac{i\omega}{2n_\omega c} P^{(3)}(\omega) = \frac{\alpha}{4} \frac{i\omega}{2n_\omega c} \chi^{(3)} d_{gr} E_{in}^3 \tag{3.5}$$

where α=1 for THG. The relation between the field and the corresponding average power is

$$P_{in/out} = \frac{1}{8} \left(\frac{\pi}{\ln(2)}\right)^{\frac{3}{2}} f \tau W^2 n_\omega \varepsilon_0 c \frac{|E_{in/out}|^2}{2} \tag{3.6}$$

assuming pulses with a repetition rate f, pulse duration τ, and a Gaussian spatial profile of diameter W on the sample.

Expressing the electric field strength through power yields

$$E_{out} = 4\left(\frac{\ln(2)}{\pi}\right)^{\frac{3}{4}} \times \sqrt{\frac{P_{out}}{f\tau W^2 n_\omega \varepsilon_0 c}} \tag{3.7}$$

Expressing $\chi^{(3)}$:

$$\chi^{(3)} = \frac{E_{out} 8 c n_\omega}{E_{in}^3 d_{gr} \omega_{THG}} \tag{3.8}$$

This gives the values for planar graphene of $\chi^{(3)}_{\text{eff}} \approx 3.9 \times 10^{-7}$ esu. For the graphene-gold nanostructure with width $w = 200$ nm at $E_F = 0.45$ eV, irradiated with 5.5 μm light, at electron temperature of 1100 K we have $\chi^{(3)}_{\text{eff}} \approx 3.4 \times 10^{-6}$ esu. These values are in a good agreement with simulations performed by our collaborators at ICFO.

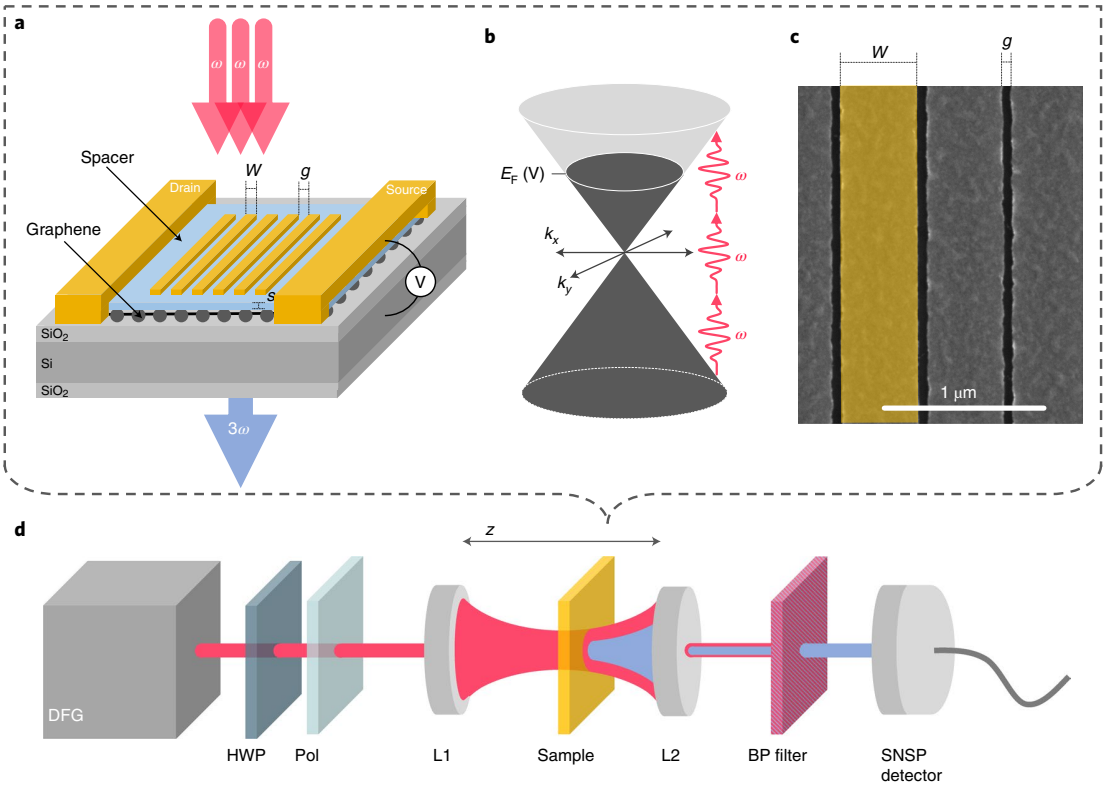

Figure 3.4: **a**, Schematic of the analyzed heterostructure.**b**, Dirac cone can be tuned into resonance with multiple incoming photons.**c**, SEM image of gold nanoribbons. **d**, The experimental setup. (24)

3.2.1 Detecting signals with SNSPD

To detect signals over a wide range of frequencies we use superconducting nanowire single photon detectors (SNSPD). The working principle of the detectors is the following. The nanowires in the detector are cooled down slightly below their critical temperature in a cryostat, then the bias current $I < I_c$ is run through the nanowires. The detector is connected to the experiment via a single or multi mode fiber. When a photon hits the nanowire it heats up above its critical temperature and superconductivity breaks. Monitoring the voltage across the wire allows for detection of photons.

3.3 Gating

Electrostatic gating is a technique used to modify electronic properties of materials by controlling their charge carrier concentrations. It is much easier to use than chemical doping, because it allows for continuous tuning of the same device over and over at different doping levels.

3.3.1 Capacitor model

One of the widely used types of gating techniques is called back-gating. To use graphene in a back-gating setup one has to create, for example, graphene/SiO_2/Si structure and connect silicon and graphene using the gating electrode. The effect of gating is then measured using metallic source-drain contacts deposited on graphene.

This device can be best modelled as a parallel plate capacitor. It accumulates equal charge of opposite sign on each of its plates. In the case of our back-gating devices, graphene and silicon play the role of parallel plates and SiO_2 is our dielectric medium. The thickness of SiO_2 defines the plate separation d. In a capacitor, the accumulated charge is proportional to the voltage applied between the plates.

The capacitance C of a parallel plate capacitor is:

$$C = \mathcal{E}_0 \mathcal{E}_R \frac{A}{d} \tag{3.9}$$

We are interested in the number of carriers of charge e per area - the surface capacitance C_S in units of $V^{-1}cm^{-2}$:

$$C_S = \frac{\mathcal{E}_0 \mathcal{E}_R}{de} \tag{3.10}$$

From this we obtain the carrier density of the graphene sheet using the difference between the applied gate voltage and the charge neutrality voltage $\Delta V = V_G - V_{CNP}$:

$$n = C_S \Delta V \tag{3.11}$$

From equation 3.11 we know that carrier concentration n is directly proportional to the applied gate voltage. The surface capacitance C_S only depends on the thickness of the dielectric and its dielectric constant according to equation 3.10.

We can optimize the ratio of these two parameters: larger capacitance requires a thinner dielectric with a stronger dielectric constant. However, using a thinner dielectric results in a lower breakdown voltage due to electron leakage, and a higher risk of sample damage. Using a stronger dielectric results in a decreased field effect, which weakens the current modulation. The ultimate goal is to reach highest possible Fermi energies using smaller voltages.

The Fermi energy is computed from charge carrier concentration:

$$E_F = \mathrm{sign}(n) \hbar v_F \sqrt{\pi |n|} \tag{3.12}$$

It is the key to creating tunable electrostatic devices. Figure 3.5 shows how applying voltages affects the distribution of charge carriers in graphene.

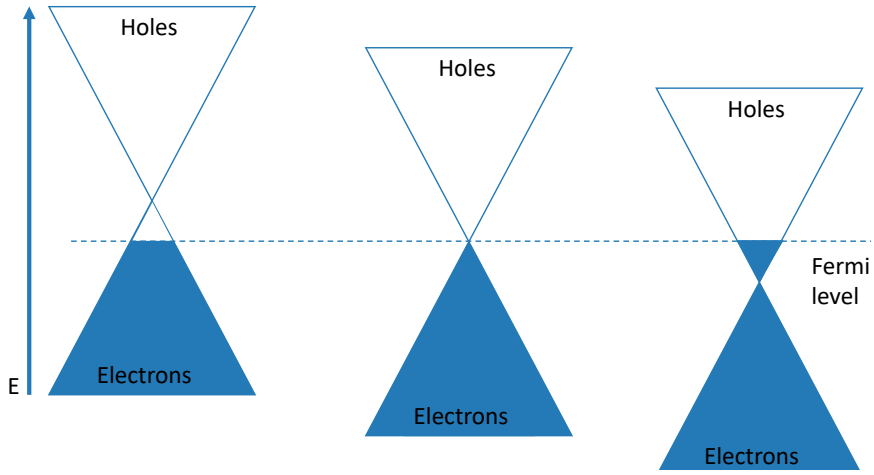

Figure 3.5: By tuning the Fermi energy using gating, one manipulates the charge distribution in graphene.

3.3.2 Sample Preparation

Another contribution I've made to the work of "Team Graphene" was setting up a graphene mini-lab for fast sample preparation. The goal was to create samples on demand, as fast as possible, with reliable electric contacts, and high production yield. The ultimate goal is to apply highest possible voltages to samples with thinnest oxide layers for achieving maximum gating efficiency.

To characterize devices, a reliable electronic setup was used. It consists of a sourcemeter connected to the lab PC and programmed to apply voltages from 0 V to $\pm$ 200 V in gate steps (typically 1 V/s). As the sourcemeter applies voltages, the current between source and drain contacts is measured.

The scheme we use for gating is the well-known back-gating scheme (figure 3.6). The gating voltage is applied between the silicon wafer and graphene, while current through graphene sheet is measured. The current between the gate contact and the drain: the "gate current" is monitored as indication of leakage through the oxide layer. One can set a current limit to avoid damaging the samples.

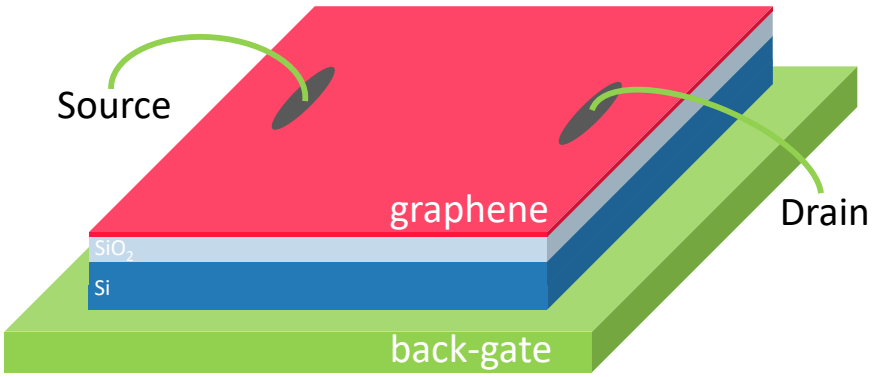

Figure 3.6: Back-gating scheme showing graphene (red) on a SiO_2/Si wafer (light and dark blue), with source and drain contacts (green) attached to contact pads (black). The back-gate in this case is a conductive plate (green) instead of a wire.

To apply back-gating voltages we use the Keithley 2450 Sourcemeter, which is connected to the chip carrier, making contact with the silicon layer on the lower side of the sample. The LabJack U6 Pro applies a voltage in the millivolt range between the source and the drain for sensing the current modulation. The source goes through a 1 kΩ resistance and connects to the analog output of the Labjack, which also sends the data to the lab computer. The drain contact goes through the low noise current amplifier DLPCA-200, which converts the small current into a usable voltage, read by the analog input of the Labjack. We use the Labjack both to apply the small source voltage, and read the output of the amplifier. Figure 3.7 shows the circuit schematic.

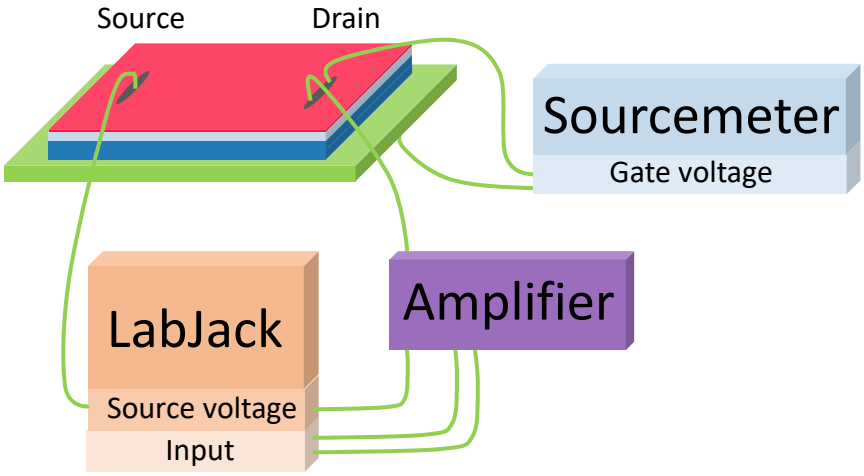

Figure 3.7: Back-gating measurement circuit schematic, where the sourcemeter applies the gating voltage, and the LabJack with the current amplifier measure the current modulation.

If the setup works properly we can see current modulation in the graphene layer, which indicates a change in resistivity. In this case the gate current stays relatively flat indicating no leakage through the oxide. If the gating device has flaws we either see no current modulation (which typically means the gating contact is not attached) or we see rapidly growing gate current (indicating current leakage, most likely due to a bad contact).

Instead of waiting for the sample to burn, we set a limit on the gate current $I_g = 100$ nA. The source meter is programmed to keep the gating voltage below the last value as the gate current reaches the limit, before we manually let it go back down to 0 V in gate steps. This limit was set by our collaborators at ICFO in our previous gating experiments. We haven't changed it since then.

We started by making the simplest back-gating device. One basic electric wire attached using silver epoxy to the back of the sample, two wires attached to the front (figure 3.14 in Appendix). The sample used was CVD gaphene on top of 300 nm thick SiO_2/Si produced by Graphenea. All samples leaked below 10 V. We then made an assumption, that the quality of contacts was poor. Specifically, that the back-gating contact has to be more uniform and requires a larger contact area.

Next we changed both: the back-gate wire was replaced by the chip carrier, the front source and drain contacts were replaced by evaporated gold pads, that were wirebonded to the chip-carrier (figure 3.16 in Appendix). This time the back-gating contact was made by putting a blob of silver epoxy in the cavity of the chip-carrier and pressing the sample against it. The blob would then turn into an almost perfect circle of approximately equal thickness, creating the largest possible contact area. The wirebonded gold pad was supposed to become a more

uniform, predictable and robust replacement for thick wires. All samples leaked below 7 V. When bonding the wire to the gold pad we unavoidably caused damaged to the gold sheet (figure 3.17 in Appendix). At lower power/duration settings of the wirebonder the wire wouldn't bond to the gold surface, at higher settings it would bond, but would also destroy the pad. To make the pads more robust we tried increasing the gold layer thickness to several hundreds nanometers, and added a titanium layer under the gold pads. We still couldn't wirebond to gold-on-titanium without making holes. So we made an assumption, that these disruptions in the gold layer create inhomogeneous electric field, that breaks through the oxide. We then added an additional step to the wirebonding: all wirebonded contacts were now covered with silver epoxy (figure 3.18 in Appendix). The idea was to reverse the damage done by wirebonding by creating a uniform field through closing the holes with relatively homogeneous conductive blobs. Still none of the samples could pass the 10 V threshold. We also tested this method using wafers without graphene getting the same result.

The next manufactured device was the same kind of Graphenea samples in a chip-carrier but this time we went back to using basic electric wires and silver epoxy for front contacts (figure 3.15 in Appendix). This time all samples leaked below 15 V. We then made an assumption, that something should be wrong with the Graphenea samples. In these samples graphene covers the whole oxide sheet. We thus assume, that at Graphenea they first cover an entire SiO_2/Si wafer with CVD graphene and then dice it into 10 mm $\times$ 10 mm samples. If this is true, pieces of graphene could be hanging over the edge of the oxide layer making contact to silicon.

After the results described above we decided to make a step back and simplify our devices. The first step was to analyse wafers without graphene to make sure they work as expected.

We then tried a setup using SiO_2/Si wafers with 90 nm oxide thickness. This time the sample reached the minimal required threshold set at 50 V by burning at 57 V. However, the thick wires were easy to move, creating disruptions in the epoxy blob. All contacts that were mechanically moved had their threshold voltage greatly reduced.

The next big step was to make a sample in a chip-carrier with the combined benefits of silver epoxy contacts and robust wirebonded wires. We have realized, that for reaching the threshold of 50 V we need to make connections without sharp edges on the contact surface. The problem now was that wirebonding to the silver epoxy is impossible, since dry epoxy does not have the right hardness for applying ultrasound to it. The tip of the wirebonder would poke holes in the dry epoxy layer, which look like chewing gum, rather than a solid. We then learned to use a tweezer to break the wire over the blob of dry epoxy, afterwards covering the wire with more epoxy from top (figure 3.19 in Appendix). Now we had an undamaged homogeneous contact thanks to viscous epoxy and robust wires thanks to the wirebonder. The new threshold was reached: 109 V. However, the production yield was low, making devices unreliable. We couldn't make an obvious connection between contact shapes, sizes, neatness, and breakthrough voltages.

The goal was now to systematize contact types and find the most reliable ones. Since we have already reached the voltages necessary for significant current modulation we now had to improve the yield. Also, an attempt was made to use the tweezer-break technique on gold contacts using silver epoxy as a buffer. This did not prove itself to be worth the time it takes to evaporate contacts, compared to using silver epoxy "pen and paper" kind of deposition.

To improve the yield the contacts of 3 sizes were made: large, medium and small. Large ones were also thick and extremely uniform, with best surface areas. Still, none of them would reach 100 V.

The wafers used weren't handled with proper care and had scratches on them, we could see with a naked eye. We thus assume, that such low breakthrough voltages for such high-quality contacts for larger contact areas were caused by covering a scratch with epoxy, providing a shortcut for the gate current. When it came to comparing medium and small sized contacts the decision wasn't so obvious. Since we had to compare breakthrough voltages of over 50 contacts, it made sense to use basic statistical methods to uncover patterns in the data.

The measurement results are summarized in figure 3.8. As can be seen in the upper chart, the new improved samples set a new record of 154 V. For us this means we could now use almost the whole voltage range available with our source meter. Since this value was obtained with an oxide of 90 nm thickness, we can now reach Fermi energies that were never available to us before.

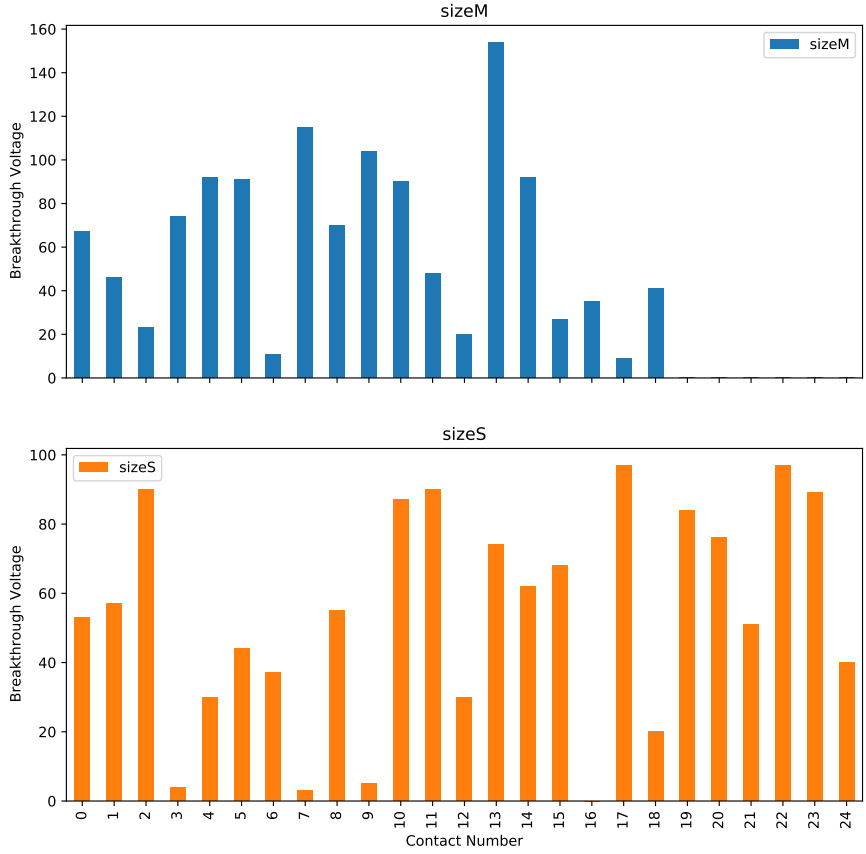

Figure 3.8: Overview of produced contacts with corresponding breakthrough voltages.

Comparing both charts in figure 3.8 we can tell, that contacts of medium size can reach higher breakthrough voltages, but seem less predictable. To make decisions about the next steps we first decided to compare the mean voltages reached by contacts of each type. These were 63.6 V for medium contacts and 53.7 V for small contacts. Judging by the mean medium contacts seem to be a better choice. However, our goal wasn't anymore to set breakthrough voltage records, but to make reliable contacts. In this case, the mean voltage is not the right estimate, but comparing probability densities is more appropriate. The probability density analysis in our case answers the question: with what likelihood would a contact reach a certain breakthrough voltage? Figure 3.9 shows the probability of reaching a voltage normalized by the number of contacts that reached the corresponding voltage. We are most interested in the region between 50 V and 100 V, where contacts of small size are clear winners.

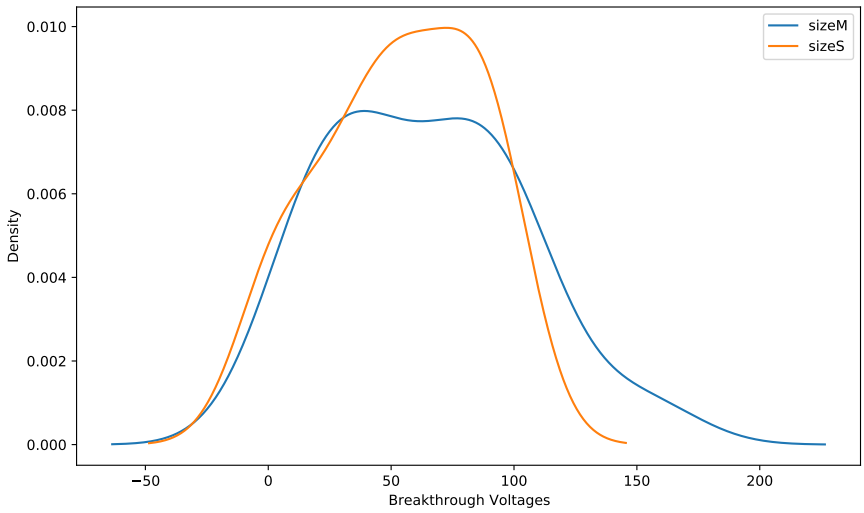

Figure 3.9: Probability density analysis.

We estimated the production yield for different voltage thresholds in the table below. Production yield is defined as the number of contacts reaching the threshold normalized by the overall number of contacts. For voltages below 60 V, contacts of small size wouldn't burn with a probability of ∼20 % higher than contacts of medium size. Above 60 V, however, contact size doesn't seem to matter anymore.

Voltage Threshold, V	sizeM %	sizeS, %
20	68	84
40	52	68
60	40	44
80	28	28

From this analysis the following conclusions were made:

- Below 60 V contact size matters. Using smaller contacts is beneficial for avoiding substrate imperfections. Contact shapes don't matter.
- If samples reach 60 V the wafer dosn't have significant imperfections (scratches for example). We can expect to reach voltages of 100 V and more, where shapes of contacts play a significal role. Having uniform round contacts with clean contact areas allows us to avoid unequal field gradients, that would break through the oxide.

The final sample with the highest yield is shown in figure 3.20 in Appendix.

After the investigation of wafers and contacts we were finally ready to deposit graphene on our devices. At this point the yield for contacts on 90 nm and 300 nm wafers was 80-90% for all voltage thresholds.

Graphene deposition was done using techniques described in the Appendix. Following the same logic used for contact preparation, graphene was cut into the smallest possible pieces using stationery scissors. After graphene deposition, the yield for 90 nm samples dropped to 18%, and for 300 nm to 73%.

To characterize the samples with graphene we first check if the applied voltage has influence on the drain current. As discussed before, the lowest charge carrier concentration corresponds

to the point of maximum resistance in a band - the charge neutrality point (CNP), also known as the Dirac Point. Being able to gate the furthest away from the CNP allows us to choose the resonant transition's frequency from largest optical spectral range. The Dirac Point (figure 1.1, figure 3.10) must be seen in the drain current measurement. An approximate value of voltage V_{CNP} required to reach the Dirac Point is also needed for further device evaluation. V_{CNP} is usually located within 20V of applied voltage, as can be seen in figure 3.10. The location of the CNP varies between devices since it largely depends on the residual doping.

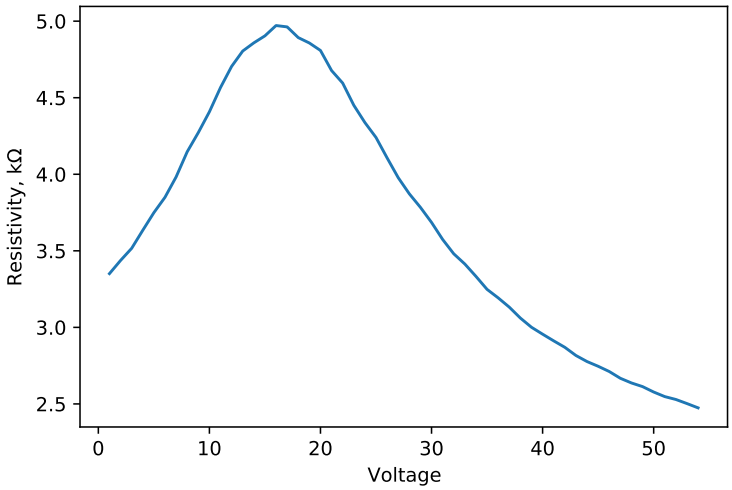

Figure 3.10: Measured resistivity of graphene sheet as a function of applied voltage. This sample clearly shows a Dirac Point at ≈ 15 V.

Next discharge measurements were used to estimate the capacitance of the devices. The measurement is very simple: we use a source meter to apply a gating voltage and measure the current between source/drain and the back-gate. The circuit schematic is shown in figure 3.11.

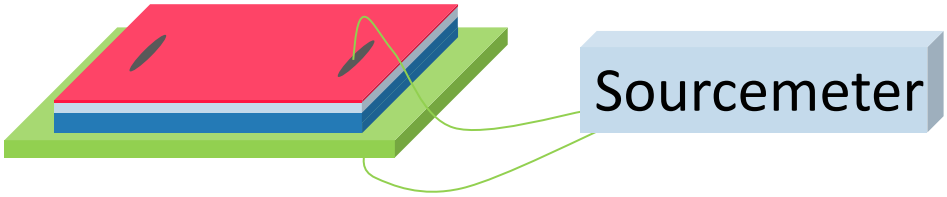

Figure 3.11: Capacitor discharge measurement scheme showing the graphene back-gating device with contact pads. Electric wires are attached to the source/drain and the back-gate, and connected to the sourcemeter.

Applying voltages between 10 and 50 V the graphene capacitor was charged, then the drop in leakage current was monitored using the source meter (figure 3.12). Basic electrostatic shielding was used to reduce the noise.

Integrating the leakage current over time gives total charge Q on the capacitor:

$$\int_0^t I(t)dt = Q \tag{3.13}$$

Dividing it by the applied voltage gives capacitance C. Then using equations 3.9-3.12 we calculate the rest of parameters from capacitance.

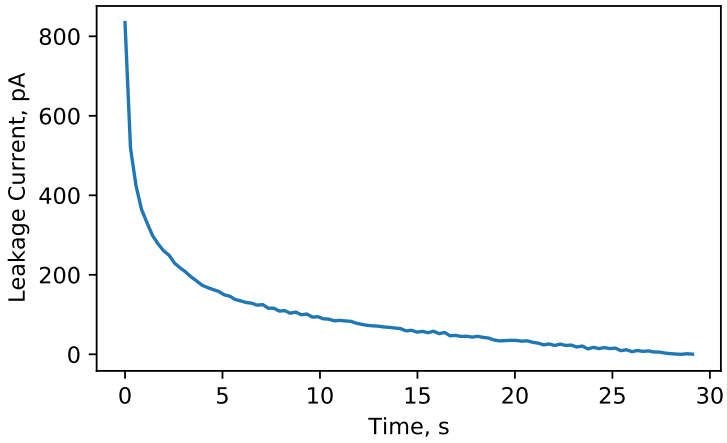

Figure 3.12: Measured leakage current.

The table below shows the characteristic parameters measured using the discharge method and calculated for samples of both oxide thicknesses. The samples with the highest performance are marked with green color.

Sample, 90 nm	Sheet area, mm^2	Capacitance, pF	Capacitor Model, pF	Surface capacitance, nF/cm^2	Carrier concentration, F/m^2	Maximum Fermi energy at V_D=100 V, eV	Maximum Fermi energy at V_D=50 V, eV
1	0.5	97	571	1.96	1e17	0.4	0.28
2	3	123	345	0.43	1e16	0.19	0.13
3	1.7	127	195	0.75	4e16	0.25	0.17
Sample, 300 nm						Maximum Fermi energy at V_D=200 V, eV	Maximum Fermi energy at V_D=100 V, eV
1	0.2	49	23	2.46	3e17	0.64	0.45
2	1	23	115	0.23	1e16	0.2	0.14
3	2.8	41	322	0.15	2e16	0.15	0.11
4	1.8	60	207	0.33	2e16	0.23	0.16
5	2.4	141	276	0.59	7e16	0.3	0.2
6	4.3	106	494	0.25	1e16	0.2	0.14
7	4.5	82	517	0.18	2e16	0.17	0.12
8	2.4	55	276	0.23	1e16	0.2	0.14
9	0.3	157	34	5.26	6e17	0.94	0.67
10	0.6	66	69	1.11	7e16	0.43	0.3
11	1.3	84	149	0.65	8e16	0.33	0.23
12	1	53	115	0.53	6e16	0.3	0.2
13	1.1	64	126	0.59	7e16	0.3	0.2
14	2.8	53	322	0.19	7e16	0.18	0.12

Table 3.1: Device characterization.

The initial goal of our project was to produce gatable samples which would at least match the samples made by our collaborators in performance of $E_F \approx 0.3$ eV. From the samples described in the above table 47% meet this criterion. The most successful devices (300 nm samples 1 and 9) even show tunabilities two and three times higher than those of our old samples.

Columns "Capacitance" and "Capacitor Model" are provided to compare the measured (capacitor discharge) and the theoretically predicted (equation 3.9) values for capacitance. With our nanostructured devices, used in section 3.2, we were able to show a good agreement between these two values. However, as can be seen in the table, for these measurements the values sometimes differ by a factor of 5. The reason is most likely in the way we measured graphene area, which plays a large role in the equation for the capacitor model. The area was measured after silver epoxy deposition, so the exact shape of the graphene sheet wasn't known anymore and we had to write down approximate values. To have the most precise values of graphene area, the area should be measured before contact deposition, using either a phone camera with a special application or a microscope. We consider the values in the column "Capacitance" more precise, because they result from a direct measurement of capacitor discharge.

Discussion

Over the last three years, I participated in various research projects and made diverse contributions, including simulations, nonlinear optical measurements, spectroscopy, and sample preparation.

The correctness of the simulation of THG versus chemical potential was confirmed by measurements in (24). This has now become the basis of our research, since every new project and every new optical setup now begins with predicting, finding, and measuring the third-harmonic signal.

The procedure I developed to prepare devices for graphene gating turned out to be a tremendous success. We can now prepare and fully characterize samples within just two working days. Also, now we don't have to restrict ourselves to the near-infrared region. The incredible tunability of these samples allows us to use the full spectral range of our laser enabling us to prove resonances in the range 1-10 μm. This opens an opportunity for research in the mid-infrared region.

Also, with the Fermi energies of our samples reaching 1 eV we can now study HHG at longer wavelengths and use the full power of Pauli Blocking. With simulations of fifth-order nonlinear current, we can now model the nonlinear response of undoped samples to light. Our collaborators are currently working on the theory for higher-order nonlinear currents in doped graphene. For future projects, we now also have a description of polarization-dependent effects. This is especially useful when nanostructured samples are being analyzed and the structure's geometry has to be matched by polarization.

Electron temperature plays a key role when measuring sharp transition resonances. Understanding and controlling it remains a challenge, which has become more approachable with available simulations. In our future projects, we will look for transition resonances while cooling down our samples to cryo temperatures and gating them. Chip carriers have to be replaced with smaller ones to fit in the cryo head, but the rest remains the same. Even the wires, that make contact with graphene are expected to remain attached thanks to the epoxy.

There are many interesting directions to go with two-dimensional materials. Further study of heterostructures with different materials and geometries could help optimize coupling and mode matching. Instead of forcing the mode volume to be confined 10^3 times in one material, we could use additional layers for gradual confinement.

Also, there is a newly emerging field of material science, that looks promising for nonlinear optics. Twisted bilayer graphene at a magic angle of 1.1° (32) has again surprised researchers launching the field of "twistronics". In twisted bilayers, the Dirac cones of both sheets overlap creating a band gap, which might amplify the optical response.

These advances help us understand the unique properties of graphene. Manipulating 2D-materials might bring us closer to nonlinear gates for photonic quantum computation.

Appendix

Sample Preparation

For the procedure described below the following wafers were used:
300 nm or 90 nm thick SiO_2 oxide on boron-doped silicon (thickness: 525 $\pm$ 20 μm, resistivity: 1-10 ohm·cm).

1. Dice the wafers. The goal is to leave as few scratches on the oxide as possible.

   Put a wafer on a tissue, measure the size of a wafer you need, take a diamond cutter, and dice the wafer. Two dicing methods are possible: either scratch a couple of millimeters into the wafer on the flat edge of the wafer or cut over the surface of the wafer from one end to the other. The first method should be safer since you don't need to touch the oxide surface at all. For the second method, you will need to use a ruler for cutting in a straight line, which is more dangerous since you can press pieces of broken quartz against the surface of oxide with a ruler creating scratches.

   If the sample didn't already break from cutting, you can break it using the ceramic coated wafer tweezers. An even better approach is to buy prediced wafers. They will be cut for you in advance, you only need to break the wafers along the lines.

2. Sonicate the sample wafers in IPA for several minutes and dry on a tissue.

3. Cut easy-transfer graphene into pieces. For the experiment described above it was done with basic stationery scissors.

4. Transfer graphene on the sample wafers. The goal is not to damage graphene by ripping or folding it.

   Graphene used in gating experiments was "Easy Transfer: Monolayer Graphene on Polymer Film" from Graphenea.

   Put deionized water into a clean glass beaker. Take the piece of graphene on PMMA with a tweezer. Carefully put it into the water under an angle to let graphene separate from the PMMA starting with an edge, until it separates completely.

   Take the sample wafer with a tweezer and put it underwater under an angle. It's easiest to catch graphene with an edge before you pull it out of the wafer. If graphene's orientation on the wafer doesn't match your plan, you can always detach it from the wafer by putting it back in the water and catching it again. Some graphene islands might still drift on the wafer if there is still water under them. You may carefully move them around on the wafer with a tweezer without applying pressure.

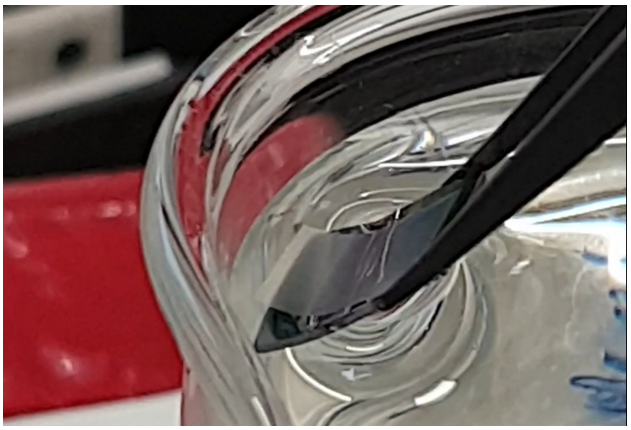

Figure 3.13: Graphene fishing.

5. Put the wafers with graphene on microscope slides and on a hot plate. It's okay if there is still water or between graphene and the sample.

   Set the temperature to 80° C and wait for about 15 minutes till the water evaporates from below graphene. Set the temperature to 130° C and wait for 15 more minutes.

6. Pour acetone into a glass beaker and carefully put the samples in acetone for 20 hours.

   If you are not careful enough graphene might detach from the wafer. Catching it in acetone might not be possible. Some acetone might evaporate during this time, so put a lot of acetone or cover the beaker to make it air-tight.

   Remove the samples from the beaker and dip them in IPA to remove the acetone residue.

7. Measure the area of graphene islands for capacitance estimation.

8. Mix the silver epoxy on a microscope slide with a ratio of epoxy to hardener of 1:1. Make contacts within 20 minutes, before the mixture hardens. It's best to make contacts within the first 10 minutes after mixing it because the epoxy is less viscous and allows for cleaner contacts.

   The silver epoxy used was CircuitWorks 60 Minute Conductive Epoxy (CW2460). In the first experiments, it was dried at room temperature for at least 24 hours. In the latter experiments, a Stuart UC 150 hot plate was used. The samples were cured at 100° C for at least 20 minutes, as specified by the manufacturer.

   If you want to reuse your PCB / chip carrier you can detach the sample from it using acetone. If you dry the epoxy at room temperature the samples can be easily detached from the chip carrier by immersing them in acetone for a couple of hours. If you use the hot plate, you will need to keep them in acetone for a couple of days, you may also never be able to detach the samples (up to 30% of them).

   To make the gate contact, put a blob of silver epoxy on the inner cavity of the chip carrier. Then drop your sample on the epoxy blob and carefully press it down with a teflon coated tweezer. The goal is to have a nice round-shaped layer of epoxy with a uniform contact area between the silicon and the chip carrier cavity. If the epoxy goes over the edge of the sample it's not a problem, unless it touches graphene. If you want to remove

some epoxy from the sample surface use a tiny piece of tissue covered in acetone to wipe the sample with a tweezer. Do not touch graphene, or you can damage it.

Make sure to position your sample in such a way, that graphene islands are as close as possible to the chip carrier contacts because wirebonding over larger distances is way harder (although still possible).

Harden the epoxy on the back-gate before making the surface contacts.

Now you should have samples with graphene on top of a wafer, attached to the chip carrier from behind with silver epoxy.

9. Prepare a new mixture of silver epoxy. Using a sharp tip (like the one on the stick for epoxy mixing) make epoxy buffer pads on graphene. It is best to place them on the edge of the graphene island in order not to touch the graphene with a sharp tip.

   It's best to make the buffer pads round-shaped with uniformly distributed epoxy. The buffer pad should be half on graphene, half on the wafer.

   Harden the buffer pads by placing the samples on the hot plate, like it was done for the back-gate. It is best not to harden them too much, since having them rock-solid will make wirebonding difficult. The texture should be like the one of chewed chewing gum. For this restrict the heating to 10-15 minutes.

10. Set the wirebonder parameters to:

    Bond 1: US $=$ 440, Time $=$ 100, Force $=$ 25,
    Bond 2: US $=$ 440, Time $=$ 100, Force $=$ 80,
    Temperature $=$ 30, Tail $=$ 160, Feed ± 15.

    Bond 1 will be used to make contact with the chip carrier. If the carrier is dirty, the wire won't attach with this little force. You can try to break through the dirt setting the force up to 80. The parameters of the second bond don't matter much. Making the force of the second bond higher than 100 will lead to deeper holes in the buffer pads. This is not very dangerous but makes it less tidy.

11. It's best not to drink coffee or energy drinks some hours before this procedure. Also, avoid bicep and forearm workout in the morning before the procedure. Shaking hands might make it impossible for you to use this technique. It's not a joke by the way.

    To use the tweezer-break technique make the first bond to the chip carrier, then pull the wire till it reaches the epoxy buffer pad. Press the needle down into the buffer pad. Without lifting the needle, take a thin curved tip tweezer. To avoid ripping the wire with a tweezer with shaky hands (even if you took the necessary percussion you might still see them shake under the microscope), press the tweezer against the wirebonder needle, slide the tweezer down along the needle, until you carefully press the wire against the buffer pad with the tweezer. Keep pressing the wire, while lifting the wirebonder needle. Now the wire should be broken over the buffer pad, while still being attached to the chip carrier.

    It's best to have two wires broken over the same buffer pad and connected to the same contact pad on the chip carrier. Do not wiggle or shuffle the tweezer over the wire or the

other end of the wire might detach from the chip carrier contact.

If your buffer pad is soft enough, you may, however, press the wire into the buffer pad, applying a lot of force, to make it stick to the buffer pad. I often did this to make the next step easier.

Also, when making long-distance bonds with a large separation between the chip carrier and the buffer pad it's best to make the wire stick in the pad, or else the wire will curl up and it will be very hard to make it go back down. If this happens, however, you may carefully press it down with a tweezer, by pressing it down next to its origin: right next to the chip carrier contact.

Repeat for each buffer pad.

12. Prepare a new mixture of silver epoxy. Release some additional wire from the needle and dip it into the mixture.

    Try not to get the needle dirty. If you do get it dirty, remove the needle from the wirebonder, put it in a glass beaker, and sonicate it in acetone for 2 minutes.

    Using the wire, covered in silver epoxy, make small blobs of epoxy, connecting the free-hanging end of the tweezer-broken wire with the buffer pad. It must be way easier if you pressed the wire into the buffer pad.

13. Cure the samples on the hot plate at 100° C for 30 minutes and let them cool down.

Pictures of samples

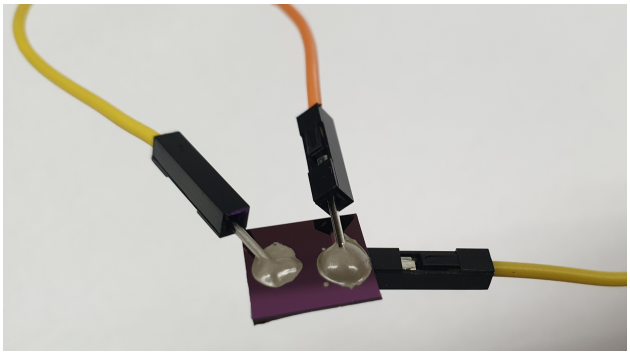

Figure 3.14: First gating attempt.

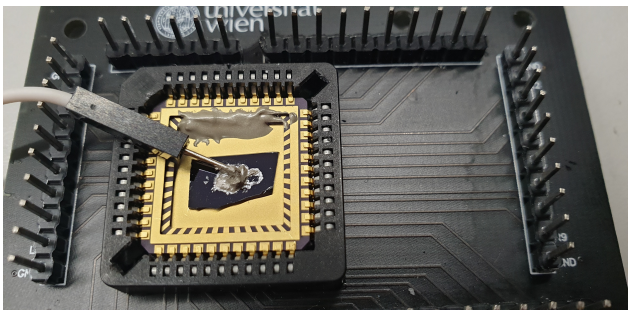

Figure 3.15: Improving the back-gate.

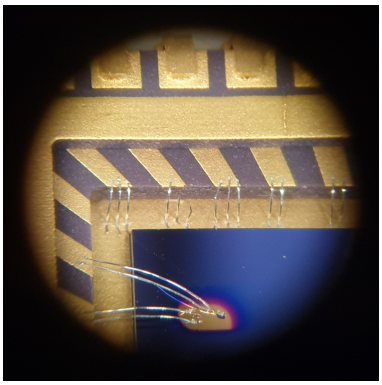

Figure 3.16: First evaporated gold pads with wirebonded contacts.

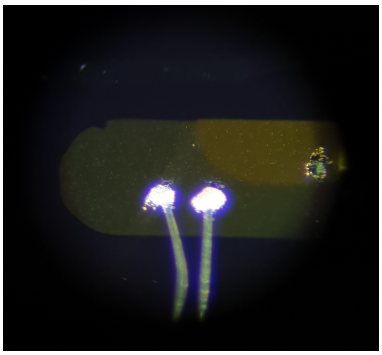

Figure 3.17: Damage done to the gold pads by the wirebonder.

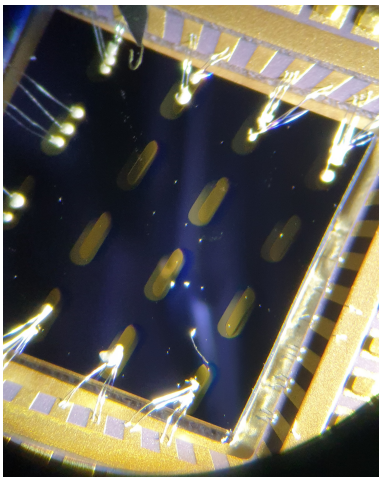

Figure 3.18: Curing contacts with silver epoxy.

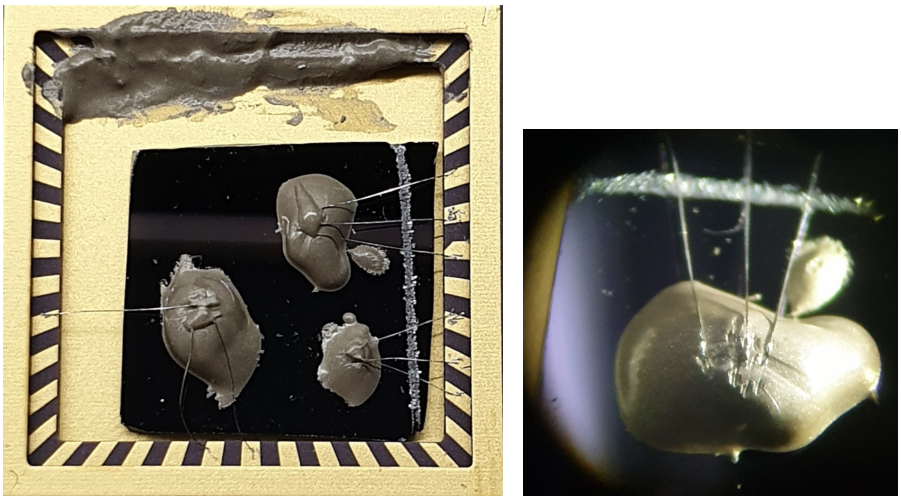

Figure 3.19: First sample with tweezer-broken wires and a closeup picture.

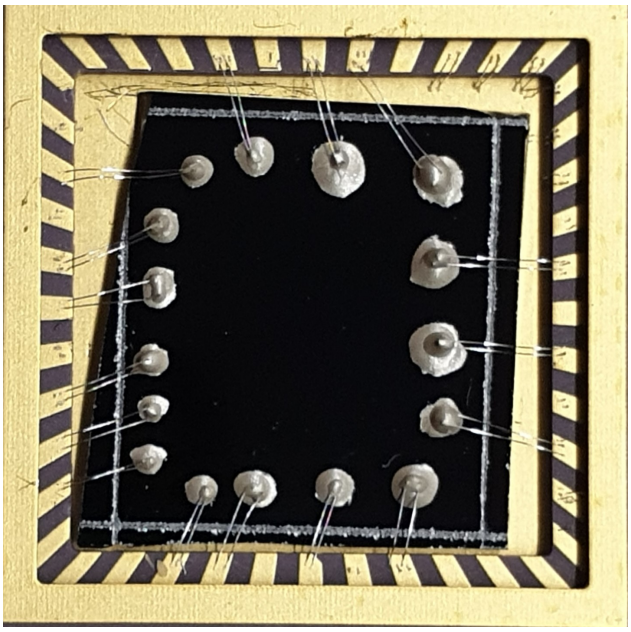

Figure 3.20: Sample with highest yield.

Simulation Codes

Dependence of third-order susceptibility of graphene on chemical potential

```
import numpy as np, math as m
from matplotlib import pyplot as plt
from scipy import constants, integrate as integrate
from scipy.constants import c, hbar, pi, epsilon_0, e, h

kB = constants.value('Boltzmann constant in eV/K')
```

```
v_f = c/300 # Fermi velocity
d_gr = 0.33 *1E-9 # graphene thickness

sigma_0 = e**2/(4*hbar) # universal conductivity
sigma_3 = sigma_0*(hbar*v_f*e)**2/pi # third-order conductivity

lambda_ = 3900*1E-9 # wavelength in nm

w_t = 3*c/lambda_
E_pump = h*c/lambda_/e # pump energy in eV

T = 300 # electron temperature
beta = 1/(kB*T)

plasmon_lifetime = 25*1E-15 # the lifetime of graphene plasmons according to ICFO
damping_from_lifetime = 1/plasmon_lifetime*hbar/e # damping as 1/lifetime
Gamma_i = Gamma_e = damping_from_lifetime
```

```
mu = np.linspace(0,-1, num = 1000)

def G1(x):
    return 1/(1+np.exp(beta*(x-mu)))*(1-1/(1+np.exp(beta*(x-mu))))*(np.
 ↪log(abs((2*abs(x)+E_pump+1j*0.2*abs(x))/(2*abs(x)-E_pump-1j*0.
 ↪2*abs(x))))+1j*(pi+np.arctan2(np.real(E_pump+1j*0.2*abs(x))-2*abs(x),np.
 ↪imag(E_pump+1j*0.2*abs(x)))-np.arctan2(np.real(E_pump+1j*0.
 ↪2*abs(x))+2*abs(x),(np.imag(E_pump+1j*0.2*abs(x))))))
def G2(x):
    return 1/(1+np.exp(beta*(x-mu)))*(1-1/(1+np.exp(beta*(x-mu))))*(np.
 ↪log(abs((2*abs(x)+2*E_pump+1j*0.2*abs(x))/(2*abs(x)-2*E_pump-1j*0.
 ↪2*abs(x))))+1j*(pi+np.arctan2(2.*E_pump-2*abs(x),0.2*abs(x))-np.
 ↪arctan2(2*E_pump+2*abs(x),0.2*abs(x))))
def G3(x):
    return 1/(1+np.exp(beta*(x-mu)))*(1-1/(1+np.exp(beta*(x-mu))))*(np.
 ↪log(abs((2*abs(x)+3*E_pump+1j*0.2*abs(x))/(2*abs(x)-3*E_pump-1j*0.
 ↪2*abs(x))))+1j*(pi+np.arctan2(3.*E_pump-2*abs(x),0.2*abs(x))-np.
 ↪arctan2(3*E_pump+2*abs(x),0.2*abs(x))))
def H2(x):
    return 1/(1+np.exp(beta*(x-mu)))*(1-1/(1+np.exp(beta*(x-mu))))*(1/
 ↪(2*abs(x)-2*E_pump-1j*0.2*abs(x))+1/(2*abs(x)+2*E_pump+1j*0.2*abs(x)))
```

```
def H3(x):
    return 1/(1+np.exp(beta*(x-mu)))*(1-1/(1+np.exp(beta*(x-mu))))*(1/
 ↪(2*abs(x)-3*E_pump-1j*0.2*abs(x))+1/(2*abs(x)+3*E_pump+1j*0.2*abs(x)))
def I3(x):
    return 1./(1+np.exp(beta*(x-mu)))*(1-1/(1+np.exp(beta*(x-mu))))*(1/
 ↪(2*abs(x)+3*E_pump+1j*0.2*abs(x))**2-1/(2*abs(x)-3*E_pump-1j*0.2*abs(x))**2);

G1 = integrate.quad_vec(G1,-m.inf,m.inf)
G2 = integrate.quad_vec(G2,-m.inf,m.inf)
G3 = integrate.quad_vec(G3,-m.inf,m.inf)
H2 = integrate.quad_vec(H2,-m.inf,m.inf)
H3 = integrate.quad_vec(H3,-m.inf,m.inf)
I3 = integrate.quad_vec(I3,-m.inf,m.inf)

Gr1 = G1[0]*beta
Gr2 = G2[0]*beta
Gr3 = G3[0]*beta
Hr2 = H2[0]*beta
Hr3 = H3[0]*beta
Ir3 = I3[0]*beta
```

```
error = [G1[1], G2[1], G3[1], H2[1], H3[1], I3[1]]
print(f'Highest value of integeration error is {max(error)}')
```

```
Highest value of integeration error is 9.927081694405379e-09
```

```
G_Axxyy_r =(1j*sigma_3)/(144*(E_pump*e)**4)*(17*Gr1-64*Gr2+45*Gr3)
G_Bxxyy_r = e*Gamma_i*sigma_3/(36*(E_pump*e)**4)*(-8*Hr2/e+17*Hr3/e+3*E_pump*Ir3/
 ↪e)
G_Cxxyy_r = -(e*(Gamma_i-Gamma_e))**2*2*1j*sigma_3/(27*(E_pump*e)**5*abs(mu*e))

G_xxyy_r = G_Axxyy_r+G_Bxxyy_r+G_Cxxyy_r;

chi_3 = 1/(1.4*1E-8)*(G_xxyy_r/(-1j*w_t*epsilon_0*d_gr)) # prefactor for␣
 ↪conversion to esu
```

Dependence of third- and fifth-order current on ellipticity

```
% constants
h_SI = 6.62607015 * 10^-34;
h_bar_eV =4.135667662*10^-15;
h_bar_SI = h_SI/(2*pi);
e = 1.602176634*10^-19;
c = physconst('LightSpeed')
mu_0 = 4*pi*10^-7
v_f = c/300 ;
s_0 = e^2/(4*h_bar_SI);
s_3 = s_0*(h_bar_SI*v_f*e)^2/pi;
k = 8.617333262145*10^-5; % in eV
k_B = physconst('Boltzmann')
epsilon_0 = 8.854187817 * 10^-12; % vacuum permittivity
d_gr = 0.33 *10^-9; % graphene thickness

input_field_intensity = 0.02*10^9 % GW/cm^2
lambda = 3900*10^-9
tau = 25*10^-15

w = 2*pi*c/lambda
k = 2*pi/lambda
w_0 = v_f*k
E_0 = sqrt(input_field_intensity)

gamma = 1/tau*h_bar_SI

steps=100

phif = (0:pi*steps)
phi = phif./steps


 for j=0:pi*steps
nu = j/steps
% nu = pi/2
eta = (sin(phi)-cos(phi).*exp(i.*nu))

xi_1 = -e.^2.*E_0.^2.*(gamma-i*w)./(4.*h_bar_SI.^2.*k.^2.*(gamma+i.*(2.*w_0-w)).*↙
(gamma-i.*(2.*w_0+w)))

xi_3 = -e.^2.*E_0.^2.*(gamma-3*i*w)./(4.*h_bar_SI.^2.*k.^2.*(gamma+i.*(2.*w_0-3.*w)).*↙
(gamma-i.*(2.*w_0+3.*w)))

xi_5 = -e.^2.*E_0.^2.*(gamma-5*i*w)./(4.*h_bar_SI.^2.*k.^2.*(gamma+i.*(2.*w_0-5.*w)).*↙
(gamma-i.*(2.*w_0+5.*w)))



n_0 = -gamma./(gamma-real(2.*abs(eta).^2.*xi_1+(2.*abs(eta).^4.*xi_1^2.*((gamma-4*i*w-↙
abs(eta).^2.*(xi_3+xi_5)).*(abs(eta).^2.*xi_5-gamma+6*i*w)+abs(eta).^4.*xi_5.^2))./↙
((gamma-2*i*w-abs(eta).^2.*(xi_1+xi_3)).*((gamma-4*i*w-abs(eta).^2.*(xi_3+xi_5)).*(abs↙
(eta).^2*xi_5-gamma+6*i*w)+abs(eta).^4.*xi_5.^2)-abs(eta).^4.*xi_3.^2.*(xi_5.*abs↙
(eta).^2-gamma+6*i*w))))

n_2 = -2.*conj(eta).^2.*xi_1.*n_0.*((gamma-4*i*w-abs(eta).^2.*(xi_3+xi_5)).*(abs(eta).↙
```

```
^2.*xi_5-gamma+6*i*w)+abs(eta).^4.*xi_5.^2)./((gamma-2*i*w-abs(eta).^2.*(xi_1+xi_3)).*
((gamma-4*i*w-abs(eta).^2.*(xi_3+xi_5)).*(abs(eta).^2.*xi_5-gamma+6*i*w)+abs(eta).^4.
*xi_5.^2)-abs(eta).^4.*xi_3.^2.*(abs(eta).^2.*xi_5-gamma+6*i*w))

n_4 = -conj(eta).^2.*xi_3.*(abs(eta).^2.*xi_5-gamma+6*i*w).*n_2./((gamma-4*i*w-abs
(eta).^2.*(xi_3+xi_5)).*(abs(eta.^2).*xi_5-gamma+6*i*w)+abs(eta).^4.*xi_5.^2)

n_6 = conj(eta).^2.*xi_5./(abs(eta).^2.*xi_5-gamma+6*i*w).*n_4


f = h_bar_SI.*k./(e.*E_0).*xi_3.*(eta.*n_4-conj(eta).*n_2)
g =  h_bar_SI.*k./(e.*E_0).*xi_5.*(eta.*n_6-conj(eta).*n_4)



THGcurrent_functionx =-sin(phi).*f
THGcurrent_functiony =cos(phi).*f
THGcurrent_integral(1,j+1) = abs(trapz(phi,THGcurrent_functionx));
THGcurrent_integral(2,j+1) = abs(trapz(phi,THGcurrent_functiony));

FHGcurrent_functionx =-sin(phi).*g
FHGcurrent_functiony =cos(phi).*g
FHGcurrent_integral(1,j+1) = abs(trapz(phi,FHGcurrent_functionx));
FHGcurrent_integral(2,j+1) = abs(trapz(phi,FHGcurrent_functiony));

 end


THGabs_current = THGcurrent_integral(1,:).^2+ THGcurrent_integral(2,:).^2
FHGabs_current = FHGcurrent_integral(1,:).^2+ FHGcurrent_integral(2,:).^2

figure
nu_plot=(0:1/steps:pi);
semilogy(nu_plot, THGabs_current/max(THGabs_current),'LineWidth',1.5)
hold on;
semilogy(nu_plot, FHGabs_current/max(FHGabs_current),'LineWidth',1.5)
axis([0 3.14 10E-8 1])
legend('3rd-order current','5th-order current')
xlabel('Polarization angle \vartheta')
ylabel('Transmission intensity, a.u.')
```

Bibliography

[1] M. Gullans, D. E. Chang, F. H. L. Koppens, F. J. García de Abajo, and M. D. Lukin. Single-Photon Nonlinear Optics with Graphene Plasmons. *Physical Review Letters*, 111(24):247401, December 2013. Publisher: American Physical Society. URL: https://link.aps.org/doi/10.1103/PhysRevLett.111.247401, doi:10.1103/PhysRevLett.111.247401.

[2] I. Alonso Calafell, J. D. Cox, M. Radonjić, J. R. M. Saavedra, F. J. García de Abajo, L. A. Rozema, and P. Walther. Quantum computing with graphene plasmons. *npj Quantum Information*, 5(1):37, 2019. doi:10.1038/s41534-019-0150-2.

[3] Ferenc Krausz and Misha Ivanov. Attosecond physics. *Reviews of Modern Physics*, 81(1):163–234, February 2009. Publisher: American Physical Society. URL: https://link.aps.org/doi/10.1103/RevModPhys.81.163, doi:10.1103/RevModPhys.81.163.

[4] P. B. Corkum and Ferenc Krausz. Attosecond science. *Nature Physics*, 3(6):381–387, June 2007. Number: 6 Publisher: Nature Publishing Group. URL: http://www.nature.com/articles/nphys620, doi:10.1038/nphys620.

[5] Shambhu Ghimire, Anthony D. DiChiara, Emily Sistrunk, Pierre Agostini, Louis F. DiMauro, and David A. Reis. Observation of high-order harmonic generation in a bulk crystal. *Nature Physics*, 7(2):138–141, February 2011. Number: 2 Publisher: Nature Publishing Group. URL: http://www.nature.com/articles/nphys1847, doi:10.1038/nphys1847.

[6] Hanzhe Liu, Yilei Li, Yong Sing You, Shambhu Ghimire, Tony F. Heinz, and David A. Reis. High-harmonic generation from an atomically thin semiconductor. *Nature Physics*, 13(3):262–265, March 2017. Number: 3 Publisher: Nature Publishing Group. URL: http://www.nature.com/articles/nphys3946, doi:10.1038/nphys3946.

[7] F. Langer, M. Hohenleutner, C. P. Schmid, C. Poellmann, P. Nagler, T. Korn, C. Schüller, M. S. Sherwin, U. Huttner, J. T. Steiner, S. W. Koch, M. Kira, and R. Huber. Lightwave-driven quasiparticle collisions on a subcycle timescale. *Nature*, 533(7602):225–229, May 2016. Number: 7602 Publisher: Nature Publishing Group. URL: http://www.nature.com/articles/nature17958, doi:10.1038/nature17958.

[8] Yong Sing You, David A. Reis, and Shambhu Ghimire. Anisotropic high-harmonic generation in bulk crystals. *Nature Physics*, 13(4):345–349, April 2017. Number: 4 Publisher: Nature Publishing Group. URL: http://www.nature.com/articles/nphys3955, doi:10.1038/nphys3955.

[9] Christopher T. Phare, Yoon-Ho Daniel Lee, Jaime Cardenas, and Michal Lipson. Graphene electro-optic modulator with 30 GHz bandwidth. *Nature Photonics*, 9(8):511–514, August 2015. Number: 8 Publisher: Nature Publishing Group. URL: http://www.nature.com/articles/nphoton.2015.122, doi:10.1038/nphoton.2015.122.

[10] Robert W. Boyd. *Nonlinear optics*. Academic press, 2019.

[11] G. X. Ni, A. S. McLeod, Z. Sun, L. Wang, L. Xiong, K. W. Post, S. S. Sunku, B.-Y. Jiang, J. Hone, C. R. Dean, M. M. Fogler, and D. N. Basov. Fundamental limits to graphene plasmonics. *Nature*, 557(7706):530–533, May 2018. Number: 7706 Publisher: Nature Publishing Group. URL: http://www.nature.com/articles/s41586-018-0136-9, doi:10.1038/s41586-018-0136-9.

[12] A. H. Castro Neto, F. Guinea, N. M. R. Peres, K. S. Novoselov, and A. K. Geim. The electronic properties of graphene. *Reviews of Modern Physics*, 81(1):109–162, January 2009. Publisher: American Physical Society. URL: https://link.aps.org/doi/10.1103/RevModPhys.81.109, doi:10.1103/RevModPhys.81.109.

[13] Aaron Bostwick, Taisuke Ohta, Thomas Seyller, Karsten Horn, and Eli Rotenberg. Quasiparticle dynamics in graphene. *Nature Physics*, 3(1):36–40, January 2007. Number: 1 Publisher: Nature Publishing Group. URL: http://www.nature.com/articles/nphys477, doi:10.1038/nphys477.

[14] A. K. Geim and K. S. Novoselov. The rise of graphene. In *Nanoscience and Technology*, pages 11–19. Co-Published with Macmillan Publishers Ltd, UK, August 2009. URL: https://www.worldscientific.com/doi/abs/10.1142/9789814287005_0002, doi:10.1142/9789814287005_0002.

[15] R. R. Nair, P. Blake, A. N. Grigorenko, K. S. Novoselov, T. J. Booth, T. Stauber, N. M. R. Peres, and A. K. Geim. Fine Structure Constant Defines Visual Transparency of Graphene. *Science*, 320(5881):1308–1308, June 2008. Publisher: American Association for the Advancement of Science Section: Brevia. URL: https://science.sciencemag.org/content/320/5881/1308, doi:10.1126/science.1156965.

[16] P. Bowlan, E. Martinez-Moreno, K. Reimann, T. Elsaesser, and M. Woerner. Ultrafast terahertz response of multilayer graphene in the nonperturbative regime. *Physical Review B*, 89(4):041408, January 2014. Publisher: American Physical Society. URL: https://link.aps.org/doi/10.1103/PhysRevB.89.041408, doi:10.1103/PhysRevB.89.041408.

[17] Yee Sin Ang, Qinjun Chen, and Chao Zhang. Nonlinear optical response of graphene in terahertz and near-infrared frequency regime. *Frontiers of Optoelectronics*, 8(1):3–26, March 2015. doi:10.1007/s12200-014-0428-0.

[18] Yee Sin Ang and C. Zhang. Subgap optical conductivity in semihydrogenated graphene. *Applied Physics Letters*, 98(4):042107, January 2011. Publisher: American Institute of Physics. URL: https://aip.scitation.org/doi/abs/10.1063/1.3549201, doi:10.1063/1.3549201.

[19] Naotaka Yoshikawa, Tomohiro Tamaya, and Koichiro Tanaka. High-harmonic generation in graphene enhanced by elliptically polarized light excitation. *Science*, 356(6339):736–738, May 2017. Publisher: American Association for the Advancement of Science Section: Report. URL: https://science.sciencemag.org/content/356/6339/736, doi:10.1126/science.aam8861.

[20] Matthias Baudisch, Andrea Marini, Joel D. Cox, Tony Zhu, Francisco Silva, Stephan Teichmann, Mathieu Massicotte, Frank Koppens, Leonid S. Levitov, F. Javier García de Abajo, and Jens Biegert. Ultrafast nonlinear optical response of Dirac fermions in graphene. *Nature Communications*, 9(1):1018, March 2018. Number: 1 Publisher: Nature Publishing Group. URL: http://www.nature.com/articles/s41467-018-03413-7, doi:10.1038/s41467-018-03413-7.

[21] Shumei Chen, Guixin Li, Franziska Zeuner, Wing Han Wong, Edwin Yue Bun Pun, Thomas Zentgraf, Kok Wai Cheah, and Shuang Zhang. Symmetry-Selective Third-Harmonic Generation from Plasmonic Metacrystals. *Physical Review Letters*, 113(3):033901, July 2014. Publisher: American Physical Society. URL: https://link.aps.org/doi/10.1103/PhysRevLett.113.033901, doi:10.1103/PhysRevLett.113.033901.

[22] S.-F. Shi, T.-T. Tang, B. Zeng, L. Ju, Q. Zhou, A. Zettl, and F. Wang. Controlling Graphene Ultrafast Hot Carrier Response from Metal-like to Semiconductor-like by Electrostatic Gating. *Nano Letters*, 14(3):1578–1582, March 2014. Publisher: American Chemical Society. doi:10.1021/nl404826r.

[23] Chun Hung Lui, Kin Fai Mak, Jie Shan, and Tony F. Heinz. Ultrafast Photoluminescence from Graphene. *Physical Review Letters*, 105(12):127404, September 2010. Publisher: American Physical Society. URL: https://link.aps.org/doi/10.1103/PhysRevLett.105.127404, doi:10.1103/PhysRevLett.105.127404.

[24] Irati Alonso Calafell, Lee A. Rozema, David Alcaraz Iranzo, Alessandro Trenti, Philipp K. Jenke, Joel D. Cox, Avinash Kumar, Hlib Bieliaiev, Sébastien Nanot, Cheng Peng, Dmitri K. Efetov, Jin-Yong Hong, Jing Kong, Dirk R. Englund, F. Javier García de Abajo, Frank H. L. Koppens, and Philip Walther. Giant enhancement of third-harmonic generation in graphene–metal heterostructures. *Nature Nanotechnology*, 16(3):318–324, March 2021. Number: 3 Publisher: Nature Publishing Group. URL: http://www.nature.com/articles/s41565-020-00808-w, doi:10.1038/s41565-020-00808-w.

[25] Tao Jiang, Di Huang, Jinluo Cheng, Xiaodong Fan, Zhihong Zhang, Yuwei Shan, Yangfan Yi, Yunyun Dai, Lei Shi, Kaihui Liu, Changgan Zeng, Jian Zi, J. E. Sipe, Yuen-Ron Shen, Wei-Tao Liu, and Shiwei Wu. Gate-tunable third-order nonlinear optical response of massless Dirac fermions in graphene. *Nature Photonics*, 12(7):430–436, July 2018. Number: 7 Publisher: Nature Publishing Group. URL: https://www.nature.com/articles/s41566-018-0175-7, doi:10.1038/s41566-018-0175-7.

[26] J. L. Cheng, N. Vermeulen, and J. E. Sipe. Third-order nonlinearity of graphene: Effects of phenomenological relaxation and finite temperature. *Physical Review B*, 91(23):235320, June 2015. Publisher: American Physical Society. URL: https://link.aps.org/doi/10.1103/PhysRevB.91.235320, doi:10.1103/PhysRevB.91.235320.

[27] J. L. Cheng, N. Vermeulen, and J. E. Sipe. Third order optical nonlinearity of graphene. *New Journal of Physics*, 16(5):053014, May 2014. Publisher: IOP Publishing. doi:10.1088/1367-2630/16/5/053014.

[28] T. Tamaya, A. Ishikawa, T. Ogawa, and K. Tanaka. Higher-order harmonic generation caused by elliptically polarized electric fields in solid-state materials. *Physical Review B*, 94(24):241107, December 2016. Publisher: American Physical Society. URL: https://link.aps.org/doi/10.1103/PhysRevB.94.241107, doi:10.1103/PhysRevB.94.241107.

[29] Kim Fook Lee, Ying Tian, He Yang, Kimmo Mustonen, Amos Martinez, Qing Dai, Esko I. Kauppinen, John Malowicki, Prem Kumar, and Zhipei Sun. Photon-Pair Generation with a 100 nm Thick Carbon Nanotube Film. *Advanced Materials*, 29(24):1605978, 2017. _eprint: https://onlinelibrary.wiley.com/doi/pdf/10.1002/adma.201605978. URL: http://onlinelibrary.wiley.com/doi/abs/10.1002/adma.201605978, doi:https://doi.org/10.1002/adma.201605978.

[30] K. S. Novoselov, A. Mishchenko, A. Carvalho, and A. H. Castro Neto. 2D materials and van der Waals heterostructures. *Science*, 353(6298), July 2016. Publisher: American Association for the Advancement of Science Section: Review. URL: http://science.sciencemag.org/content/353/6298/aac9439, doi:10.1126/science.aac9439.

[31] David Alcaraz Iranzo, Sébastien Nanot, Eduardo J. C. Dias, Itai Epstein, Cheng Peng, Dmitri K. Efetov, Mark B. Lundeberg, Romain Parret, Johann Osmond, Jin-Yong Hong, Jing Kong, Dirk R. Englund, Nuno M. R. Peres, and Frank H. L. Koppens. Probing the ultimate plasmon confinement limits with a van der Waals heterostructure. *Science*, 360(6386):291–295, April 2018. Publisher: American Association for the Advancement of Science Section: Report. URL: https://science-sciencemag-org.uaccess.univie.ac.at/content/360/6386/291, doi:10.1126/science.aar8438.

[32] Yuan Cao, Valla Fatemi, Shiang Fang, Kenji Watanabe, Takashi Taniguchi, Efthimios Kaxiras, and Pablo Jarillo-Herrero. Unconventional superconductivity in magic-angle graphene superlattices. *Nature*, 556(7699):43–50, April 2018. Number: 7699 Publisher: Nature Publishing Group. URL: http://www.nature.com/articles/nature26160, doi:10.1038/nature26160.